



Walter Schottky Institut
Center for Nanotechnology and Nanomaterials
Fakultät für Physik der Technischen Universität München

Electrical Readout of NV⁻ Centers in Diamond

Felix Hartz

Master Thesis

August 2017

Contents

1. NV⁻ center in Diamond as a Future Quantum Memory Candidate	1
2. Theory	3
2.1. High Purity Single Crystal Diamond	3
2.1.1. NV Centers in Diamond	3
2.1.2. NV ⁻ Center Level Diagram and Photoluminescence Spectrum	4
2.1.3. Generation of Photocurrent in Diamond	5
2.2. Electron Spin Resonance	6
2.2.1. Rotating Frame System	7
2.3. Metal Semiconductor Metal Photodetector Operation Principle	8
3. Diamond Samples	13
3.1. Single Crystal Diamond Substrates	13
3.2. Sample Processing	13
3.3. Current-Voltage Characteristics	16
3.3.1. Photocurrent	17
4. Experimental Setup for pEDMR and ODMR Detection of NV⁻ Centers in Diamond	19
4.1. Optics	19
4.1.1. Laser Sources	19
4.1.2. Confocal Microscopy	22
4.1.3. Single Photon Avalanche Detector for NV ⁻ Fluorescence detection	24
4.2. Electronics	25
4.2.1. Low Noise Transimpedance Amplifier for Photocurrent Detection	25
4.2.2. Microwave Circuit	26
4.3. Timing Control	27
4.3.1. Excitation Pulse Sequence	28

Contents

5. Basic Experiments	31
5.1. Photoluminescence Detection and ODMR of NV ⁻ centers	31
5.1.1. Spatial Resolution of the Photoluminescence Detection	31
5.1.2. ODMR on NV ⁻ centers	33
5.2. Photocurrent Detection	37
5.2.1. Two Photon Ionization of NV ⁻ center	37
5.2.2. Characteristics of the MSM Photodetector	38
5.2.3. Mapping the photocurrent	40
5.3. Pulsed Electrical Detected Magnetic Resonance on NV ⁻ Centers	42
5.3.1. Electron Spin Resonance	43
5.3.2. Optimization of pEDMR Dynamics	46
6. Dual laser excitation of the NV⁻ center	49
6.1. 520 nm and 450 nm Dual Laser NV ⁻ Ionization	49
6.1.1. Alignment of Laser Spots	49
6.1.2. 450 nm Laser Photoionization of the NV ⁻ Center	51
6.1.3. Pulse Sequence for Green and Blue Laser Assisted pEDMR on NV ⁻ centers	53
6.2. Green Red Excitation	57
6.2.1. Laser Alignment	57
6.2.2. Dual Laser Photoionization Protocol prohibiting N _s ⁰ Ionization	59
7. Outlook and Conclusions	63
A. Laser Characteristics	67
A.1. Mathematical Discussion on Laser Calibration	67
A.2. Laser Power Calibration	69
A.2.1. Blue Laser	69
A.2.2. Green Laser	69
A.2.3. NIR Laser	69
A.3. Laser Suppression in the Photon Detection System	69

1. NV⁻ center in Diamond as a Future Quantum Memory Candidate

With increasing interest research on the diamond nitrogen vacancy (NV⁻) center has been conducted for more than a decade. Alternatives for the well understood and utilized silicon based transistor technology encountering atomic limits are quested by scientists also with both rising pressure and financial support from computer industry. As one of the more abundant defects in natural diamond it forms a paramagnetic spin triplet with excellent spin coherence times with the prospect to provide quantum information storage at room temperature Bar-Gill et al. (2013). The spin of NV⁻ centers can be manipulated thousands of times under appropriate control conditions before decoherence sets a limit to further operation. Without nuclear spins disturbing electron spin coherence silicon and diamond are candidates for implementing single qubits into semiconductor environment Muuronen et al. (2014). Isotopical enrichment of ²⁸Si or ¹²C, respectively, has crucial impact on spin coherence enlargement as long as shallow defects are not limited by electronic fluctuations from surface states Itoh and Watanabe (2014).

As a quantum sensor the NV⁻ center can be utilized demonstrating good performance and sensitivity when detecting temperature, electric or magnetic fields Acosta et al. (2010a) Maze et al. (2011) MaletinskyP. et al. (2012). The level splitting of the NV⁻ center spin in its ground state is sensitive to all three mentioned quantities and even allows to identify the field orientation with respect to the own orientation defined by one of four possible orientations in the diamond lattice. Recent studies demonstrated reconstruction of magnetic field domains from small magnetic samples attached to a diamond surface Bar-Gill and Retzker (2017).

The spin of NV⁻ centers can be read out optically with well established photoluminescence detection techniques, typically using the same objective for detection as for excitation. Outcoupling of photons from high refractive

1. NV⁻ center in Diamond as a Future Quantum Memory Candidate

diamond into air is insufficient and a variety of concepts for optimization is discussed. While Purcell effect increases the photon count rate at the cost of spin contrast, additional optics such as mirrors, micro antennas, oil and solid immersion lenses and dielectric or plasmonic grating Zheng et al. (2017), Choy et al. (2013). A very different approach to study NV⁻ center spin and charge is electrical detection with piko second resolution, when the NV⁻ center is coupled to graphene Brenneis et al. (2015). Spin selectivity is here provided by graphene where electron spin is connected to propagation direction. The defect may be read out as well by fabricating metallic top gates, effectively creating a metal-semiconductor-metal photodetector. This ansatz allows for downscaling and has been demonstrated to provide results that compare with photoluminescence detection Bourgeois et al. (2015), Hrubesch et al. (2017). The physics of electrical read out is more complex and understood as an effective four photon absorption process that can be driven at wavelengths in the visible, green spectrum. In this work I will discuss this process and possibilities for optimization. All experimental findings can be explained by a model of the NV center that is in agreement with other reports on theoretical and experimental studies.

2. Theory

2.1. High Purity Single Crystal Diamond

A wide range of diamonds exhibits notable differences in physical properties. More specifically, conduction may vary from insulating over n- or p-type bulk semiconduction to surface conduction Hauf et al. (2014). Since impurities and defects define the electrical properties as well as optical absorption, the entire field of research benefits from advanced material engineering in the chemical vapour deposition (cvd) diamond growth process Isberg et al. (2002). Further tuning the electrical structure beyond introducing impurities in the bulk through surface states enables construction of a new generation of devices based on diamond such as Field Effect Transistors (FETs) Hauf et al. (2014).

2.1.1. NV Centers in Diamond

The four carbon valence electrons form covalent sp^3 bonds Sze and Kwok (2007). The crystal structure is a face centered cubic with a two atomic base, probably better known as the diamond structure. All bonds have the same length and occur under equally distributed directions under the tetrahedral angle of 109.5° . Diamonds exhibits an indirect bandgap of 5.45 eV Sze and Kwok (2007). Due to the high binding energy of the bonds diamond holds the record in mechanical stability, heat conductivity and predicted breakdown voltages of $\sim 10\text{MV/cm}$ Isberg et al. (2002), Maze et al. (2011). In combination with the high carrier mobility fast operations even at room temperature and above scientific research interest in diamond based devices rises. Motivated by the discovery of long spin coherence time even at room temperature diamond is a possible candidate for future quantum information processing Bar-Gill et al. (2013). Naturally abundant diamonds vary in density and distribution of impurities. This led to a classification system being still used today, albeit criteria changed over time with increasing knowledge and technology progress Walker (1979). Table 2.1 gives an overview on the different diamond types.

2. Theory

type	characteristic feature	dominant impurity (cm^{-3})
I a	aggregated N	$c(N) \approx 2 \cdot 10^{18} - 5 \cdot 10^{20}$
I b	low N	$c(N) \approx 4 - 9 \cdot 10^{19}$
II a	N	$c(N) < 2 \cdot 10^{18}$
II b	hardly detectable N	$c(N) < 2 \cdot 10^{16}$

Table 2.1.: Classification of diamond types Walker (1979).

The samples used in the scope of this work were type IIa diamonds with nitrogen concentrations of $c(N) \leq 2 \cdot 10^{19}$. At room temperature and elevated temperatures carrier mobility for type IIa diamonds is limited by acoustic phonon scattering, as has been concluded from charge limited transport experiments Isberg et al. (2002). Different electron mobilities between 2000-2800 cm^2/Vs for natural type IIa diamonds and 4100 cm^2/Vs are attributed to defect-scattering mechanisms, being minimized with crystal quality Isberg et al. (2002). Due to the higher effective mass hole mobility is lower, typically by 20%. NV^- center defects are randomly distributed in the sample and occur wherever a nitrogen donor meets a carbon vacancy. In the following section the physical properties of the NV^- center will be described.

2.1.2. NV^- Center Level Diagram and Photoluminescence Spectrum

The level diagram of the NV^- center is shown in fig. 2.1 b). The ground state singlet ${}^2\text{A}$ exhibits a zero field splitting D between the spin singlet $|1\rangle$ and triplet state $|2\rangle$. Excitation with green laser light promotes the valence electron into the phonon side band of one of the first optically excited states $|3\rangle$ or $|4\rangle$. For this electrical transition (E1) spin is conserved. Relaxation to the initial states occurs with a transition rate of 15.8 ns or 15.9 ns, slightly depending on the spin. The spectral distribution of this defect as depicted in fig. 2.1 c) is known for more than two decades (Aslam et al., 2013), Gruber et al. (1997). There is another decay channel into a non photoluminescent state $|5\rangle$, also referred to as dark state. Transition rates into $|5\rangle$ strongly depend on the spin, with 77 ns for $|3\rangle \rightarrow |5\rangle$ being slower or with 13 ns for $|4\rangle \rightarrow |5\rangle$ faster than the radiative decay. However, spin coherence gets lost in this nonradiative transition. Recombination from $|5\rangle$ back to the ground state singlet manifold ${}^2\text{A}$ takes significantly longer than the prior transitions. The photoluminescence spectrum of both NV center charge states are depicted in fig. 2.1 c), adapted from (Aslam et al., 2013). Under 440 nm laser excitation the neutral charge state gets excited and relaxes by photo-

2.1. High Purity Single Crystal Diamond

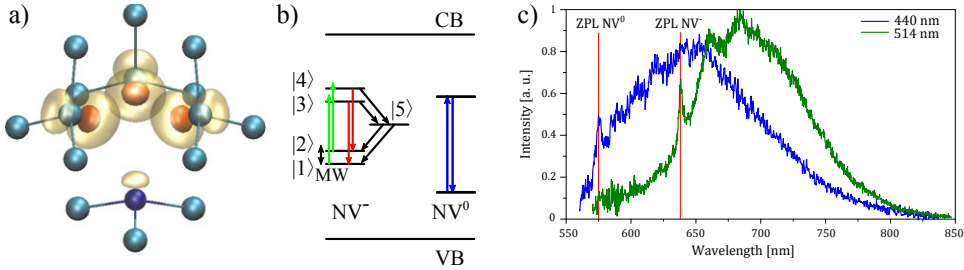


Figure 2.1.: (a) Structure of the NV^- center in diamond and the simulated spin density contour Gali (2011). b) Level scheme with indicated microwave and visual photon transitions. c) Photoluminescence diagram for both NV^0 and NV^- centers recorded with different excitation energies (Aslam et al., 2013)

luminescence. The ZPL for NV^0 can be observed as a sharp maximum at the high energy side of the spectrum, the value is reported to be 575 nm. NV^- center photoluminescence can not be detected, it becomes dominant when the laser photon energy is lower than the NV^0 ZPL and thus cannot excite NV^0 . The photoluminescence spectrum of NV^- , here recorded under 514 nm laser excitation into the phonon side band, reveals the weak ZPL at 637 nm. Emission into the phonon side band is much more probable. The spectrum is centered at about 700 nm and has a width at half maximum of about 80 nm.

2.1.3. Generation of Photocurrent in Diamond

Ionization of the NV^- center occurs when the energy of exciting photons exceeds the ZPL transition energy. A process including three photons is considered to drive the ionization as has been proposed by Siyushev et al. (2013).

In fig. 2.2 a) the NV center level structure and the individual excitation steps are depicted. Here the ground state a_1 corresponds to the states $|1\rangle$ and $|2\rangle$. From there a first photon promotes one electron into the first optically excited state. A second photon lifts this photon into the conduction band before any possible recombination into the ground or dark state. From density functional theory simulations it is conducted, that an Auger process

2. Theory

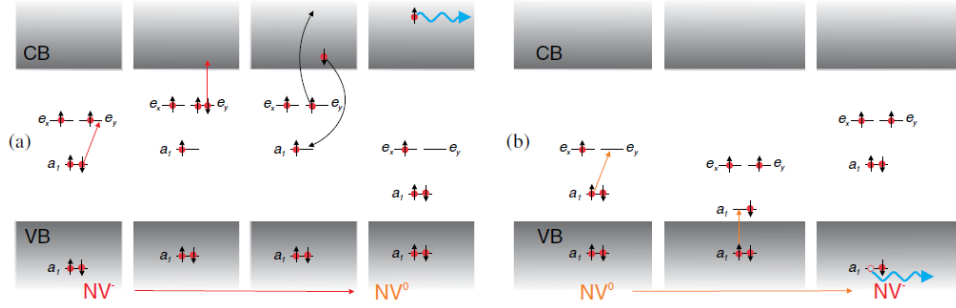


Figure 2.2.: (a) Ionization of the NV^- center by two photon excitation. b) The initial negative charge state is recreated by two photon excitation of a valence band electron Siyushev et al. (2013). Energy level differences for varying orbital occupation or charge-state are illustrated schematically.

takes place on a faster timescale than recombination. After the Auger process the electron has a sufficient energy to leave the defect. The timescales for recombination decreases with photon energy, making the Auger process more improbable for higher energies. When the conduction band electron has escaped, the defect is in its neutral state NV^0 . Under illumination the initial negative charge state is recovered, as shown in fig. 2.2 b). A electron of the ground state in the band gap is excited and refilled by another valence band electron. This leaves a hole state in the valence band which can propagate to a contact. We end up after one cycle with the initial NV^- state having created a free electron and a free hole.

2.2. Electron Spin Resonance

Six electrons build up the the NV^- center in diamond exhibiting a spin of one. For the magnetic interaction of the spin with its environment one considers the spin Hamiltonian in the optical ground state. It is the sum of the Zeeman energy and a contribution from the crystal magnetic field Christle et al. (2015)

$$H = \mu_b g \mathbf{S} \mathbf{B}_0 + \mathbf{S} \hat{\mathbf{D}} \mathbf{S} \quad (2.1)$$

where g denotes the g factor of the electron, μ_b the Bohr magneton, \mathbf{D} the zero field splitting tensor and \mathbf{S} the total electron spin. In absence of any magnetic field the Zeeman term vanishes and one obtains

$$H = D \left(S_z^2 - \frac{1}{3} S(S+1) \right) + E(S_x^2 + S_y^2) \quad (2.2)$$

2.2. Electron Spin Resonance

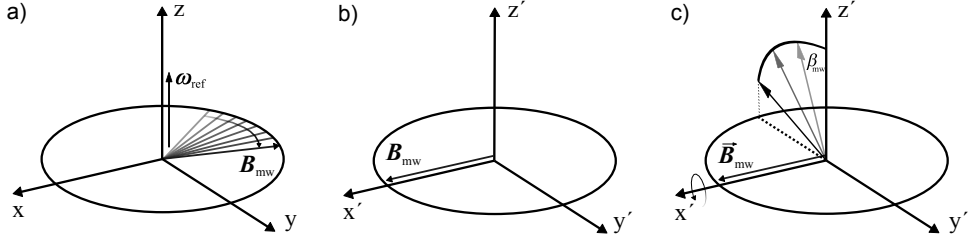


Figure 2.3.: (a) In the laboratory frame system \vec{B}_{MW} precesses, whereas (b) \vec{B}_{MW} has a time independent representation in a rotating frame system where ω_{ref} is set to ω_0 . c) A microwave pulse rotates the Spin state along the x axis into another z projection state.

with the zero field splitting parameter $D = 3/2 D_{zz}$. For crystals like diamond with C_{3v} symmetry there is no anisotropy field and thus $E = 0$, simplifying eq. (2.2) to Christle et al. (2015)

$$H = D \left(S_z^2 - \frac{1}{3}S(S+1) \right) \quad (2.3)$$

Finally we expect for the different spin states with the projections $S_z = 0$ and $S_z = \pm 1$ an energy difference of D .

2.2.1. Rotating Frame System

So far we have discussed spin precession in a constant magnetic field. Transitions between spin states can be induced by microwave photons of the right frequency and polarization. In this section the mathematical representation of the spin state will be discussed under the influence of an additional magnetic microwave field. The Schrödinger equation of a spin system being driven by a time dependent magnetic field B_{MW} shows a time dependence as well. By appropriate choice of coordinate system this time dependence disappears. This is the case for coordinate axes rotating along the quantization axis z with Larmor frequency ω_0 , as illustrated in fig. 2.3.

$$\hat{\tilde{H}}_0 = \omega_{\text{nut}} \hat{I}_x \quad (2.4)$$

with

$$\omega_{\text{nut}} = \left| \frac{1}{2} \gamma B_{\text{MW}} \right| \quad (2.5)$$

2. Theory

The operator \hat{I}_x just rotates the spin state along the x axis by a rotation angle β_{MW} for a constant magnetic field over time t_{MW}

$$\beta_{\text{MW}} = \omega_{\text{nut}} t_{\text{MW}}. \quad (2.6)$$

Experimentally spin transitions are of interest in this work, thus the rotation by $\beta_{\text{MW}} = \pi$. The corresponding interaction time can be estimated from the experimentally available magnetic field that is provided by a gold wire. It has a diameter of $70 \mu\text{m}$ and is placed close to the interdigital contact structure. In reality the skin effect defines the penetration depth in metals, described by the skin depth δ_{skin} as characteristic constant. The choice of the wire radius is a trade-off between high radiation efficiency, a large cross section for current transport at microwave frequencies and small wire to probe volume distance to maximize the magnetic field. For simplicity an infinitely thin wire is considered here, resulting in an underestimate for the real magnetic field. From the Biot-Savart law one can derive easily the magnetic field B for the two-dimensional and radial-symmetric case

$$B_{\text{MW}}(R) = \frac{\mu_0 I}{2\pi R}. \quad (2.7)$$

Here, R denotes the distance from the center of the wire and I the total current through the wire. Neglecting the direct current (DC) resistance and using the impedance $R_z = 50 \Omega$ one obtains

$$B_{\text{MW}}(R) = \frac{\mu_0 \sqrt{P/R_z}}{2\pi R} = \frac{\mu_0 \sqrt{10 \text{ W}/50 \Omega}}{2\pi \cdot 70 \text{ nm}} = 1.3 \text{ mT}. \quad (2.8)$$

Using equations 2.5 and 2.6 we can convert B_{MW} into $\omega_{\text{nut}} = 2.9 \text{ MHz}$ and finally obtain for the spin transition time $t_{\text{MW}} = 170 \text{ ns}$.

2.3. Metal Semiconductor Metal Photodetector Operation Principle

Experimentally the task is to detect photocurrent generated in bulk diamond. Evaporated metallic contacts on the diamond surface allow basically for electrical detection of the photocurrent when a bias voltage is applied to the device. The device concept used is known as metal insulator metal (MSM) photodetector. In this section I will discuss the relevant physical properties and limits of the self-assembled MSM detectors.

The general device structure consists of interdigital contacts directly on the

2.3. Metal Semiconductor Metal Photodetector Operation Principle

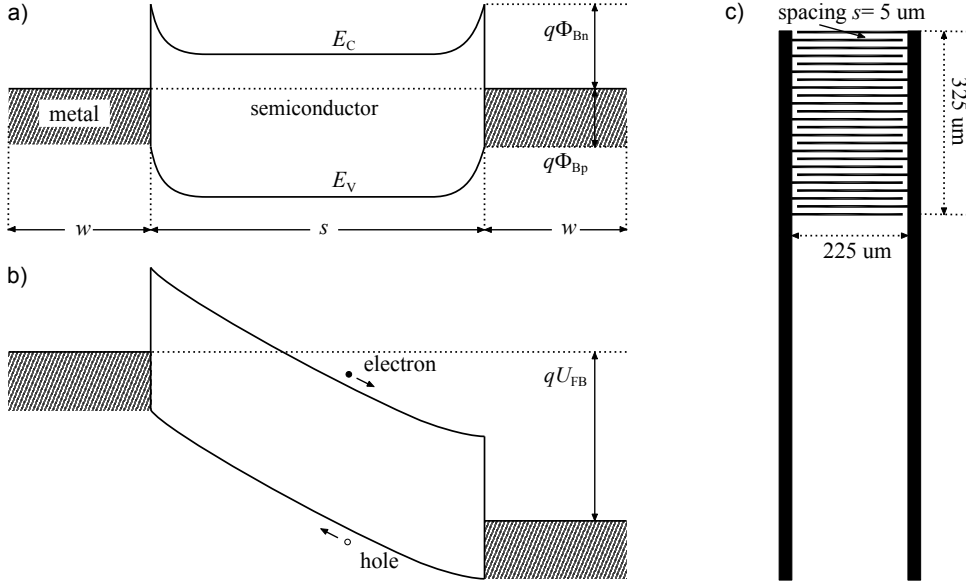


Figure 2.4.: Band level scheme for a MSM photodetector in a a) unbiased configuration and for b) flat-band condition, where the electric field at the anode becomes zero. c) MSM detector layout with 24 interdigital contacts.

sample surface, eventually with a barrier enhancing layer in between Sze and Kwok (2007). In the region between contacts a volume of detector material is illuminated and charge carriers are excited. In biased operation mode a depletion region is build at the anode effectively separating the generated charge carriers. Under the influence of electrical field they drift to the contacts. This process is illustrated schematically in fig. 2.4.

With increasing bias voltage the depletion region expands. In one dimensional approximation the depletion region w can be calculated as Sze and Kwok (2007)

$$w = \sqrt{\frac{2\epsilon_s U_b}{qN}}. \quad (2.9)$$

Here ϵ_s and N denote the effective dielectric constant and the doping density respectively. The depletion region increases with the square root of the bias voltage U_b . A saturation of photocurrent is expected when the entire region between two contacts is depleted by a voltage U_{fb} and all generated carriers

2. Theory

are collected, mathematically expressed as

$$U_{\text{fb}} = \frac{qN}{2\epsilon_s} s^2. \quad (2.10)$$

In this case the band curvature at the anode is zero, referred to as flat band mode.

Next the speed performance of a MSM shall be considered. There are in general two limiting regimes given by the RC bandwidth or the transit time of carriers. For a series RC circuit the bandwidth f_{RC} calculates as

$$f_{\text{RC}} = \frac{1}{2\pi(R_L + R_S)C} \quad (2.11)$$

with the series and load resistances R_L and R_S respectively and the device capacitance C Sze and Kwok (2007). In case of diamond as detector material $R_S \gg R_L = 50\Omega$ allowing neglection of R_L in the calculation. The last unknown quantity C can be estimated from the device dimensions using Sze and Kwok (2007)

$$C = \frac{K(\kappa)}{K(\kappa')} \frac{\epsilon_0 A(1 + K_s)}{s + w}. \quad (2.12)$$

Here K denotes the line integral of the first kind with arguments $\kappa = \tan^2\left(\frac{\pi w}{4(s+w)}\right)$ and $\kappa' = \sqrt{1 - \kappa^2}$. Inserting the contact dimensions $s = 10 \mu\text{m}$, $w = 5 \mu\text{m}$ and an overall area of $350 \times 300 \mu\text{m}^2$ one obtains a theoretical capacity of $C = 10.4 \text{ pF}$.

The transit time limited bandwidth depends only on the material's transport property electron or hole velocity and the contact spacing Sze and Kwok (2007):

$$f_{\text{transit}} = \frac{0.44 v}{\sqrt{2} s} \quad (2.13)$$

Inserting numbers¹ into equations (2.11) and (2.13) one obtains $f_{\text{RC}} = 300 \text{ GHz}$ and $f_{\text{transit}} = 2.8 \text{ GHz}$ for a 5 V biased device. With $f_{\text{transit}} \ll f_{\text{RC}}$ the device is operated in a regime limited to majority carrier transit time. For the detection of charge carriers generated by laser pulses in the 10^1 to 10^3 ns regime corresponding to current modulations $f_{\text{mod}} \leq 0.5 \text{ GHz}$. Since $f_{\text{mod}} < f_{\text{transit}}$ usage and interpretation of the introduced MSM photodetector as a device with linear response is justified.

¹An electron mobility of $1800 \frac{\text{cm}^2}{\text{Vs}}$ is assumed Sze and Kwok (2007).

2.3. Metal Semiconductor Metal Photodetector Operation Principle

Schottky contacts on Diamond

Photoconductive Gain

Internal processes can lead to a observable current being higher than the current primarily generated by photo excitation in the detector. This subsection refers to the discussion of S.M. Sze in Sze and Kwok (2007). The current enhancing effect is described by a photoconductive gain factor

$$G = \frac{I_p}{I_{ph}}. \quad (2.14)$$

Here the current generated by a photo excitation is denoted as I_{ph} and the detected current as I_p . Electron and holes drift in a electric field to opposite contacts where they are collected. Characteristic are here the carrier density n and the carrier lifetime τ , which depends on the position of the Fermi level and the relevant relaxation process in the detector material of dimensions $A \cdot L = V$. Under constant carrier generation rate G_e the steady state condition for the carrier density is

$$n = G_e \tau \quad (2.15)$$

giving rise to a drift current in an electric field E of

$$I_p = (\mu_n + \mu_p)nqEA. \quad (2.16)$$

The primary photocurrent is just

$$I_{ph} = \frac{qG_e}{V}. \quad (2.17)$$

Inserting (2.16) and (2.17) in (2.14) yields

$$G = \frac{(\mu_n + \mu_p)\tau E}{L} = \tau \left(\frac{1}{\tau_n} + \frac{1}{\tau_p} \right). \quad (2.18)$$

Here the carrier transition times are defined as

$$\tau_{n,p} = \frac{L}{\mu_{n,p} E}, \quad (2.19)$$

scaling linearly with the distance of travel and inversely with the acceleration field below saturation.

3. Diamond Samples

3.1. Single Crystal Diamond Substrates

As substrate we use chemical vapor grown single crystal diamonds. They exhibit a homogeneously distributed nitrogen density of $c(N) < 1$ ppm or $c(N) < 5$ ppb in case of type IIa or type Ib diamond, respectively. Boron atoms with a concentration of $c(B) < 5$ ppb are not the dominant defect. NV-defects occur naturally at one percent of the nitrogen atoms in diamond. The ratio can be increased when defects in the diamond crystal are generated by irradiation with electrons (cite reference) or by nitrogen irradiation. Without external magnetic field and thus without a well defined quantization axis it is not important how the crystal is aligned with respect to the setup geometry. We are free to choose any crystal orientation. However we decide for (100) surface orientation for all of our samples. Roughness of the polished diamond surface is specified to be less than 10 nm on average. These smooth surfaces provide a well defined starting point for further processing steps. A schematic of the fabrication processes is given in figure 3.1.

3.2. Sample Processing

Within the scope of this work four diamond samples varying in defect concentration and contact fabrication have been studied. By the choice of contact material the Schottky barrier height can be adjusted. Annealing of evaporated contacts reduces the barrier height again. Engineering of the required contacts is possible, however the goal was to realize samples with Schottky and others with ohmic contacts.

Oxygen Termination of the Surface

The samples were oxygen plasma treated before and after the lithography step. This method provides a non-directional etching of surface contaminations on the diamond including hydrogen termination. Adhesion of metal contacts that are to be fabricated later on is improved as well. Dependent

3. Diamond Samples

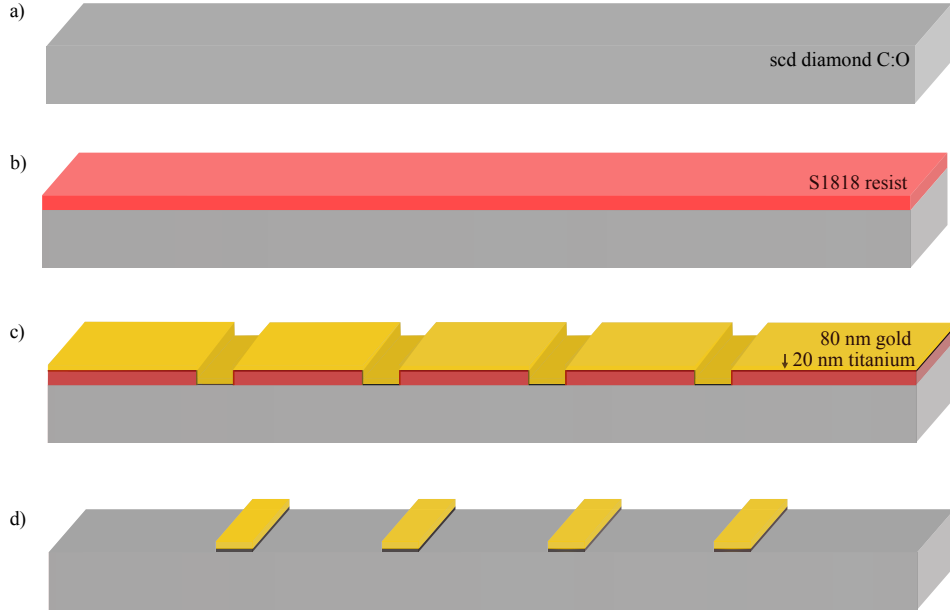


Figure 3.1.: Contact fabrication. The diamond sample (a) is covered by photoresist (b) After UV-lithography and metal evaporation (c) the interdigitated structure (d) is developed within a lift off process.

on power and duration of the microwaveplasma the shape and etching depth can be tuned. The influence of these parameters on the resulting surface quality has been investigated by and optimized Hauf et al. (2014). For the used plasma microwave reactor (*Technics Plasma GmbH* 100-E Plasma System) operation at 1.4 mbar and a power of 200 W for 300 s is the set of parameters promising good results Hauf et al. (2014).

UV-Photolithography

Metallic top contacts were fabricated using UV-photolithography. Two interdigital structures as introduced in section 2.3 with contact width of 5 μm and contact distance of 10 μm were used. Due to the limited charge carrier mobility in diamond we chose that small contact distances. Positive photoresist (*schipley* S1818) is spun at 9000 rpm for 30 s. Before the pre-bake at 90 °C for 10 min photoresist aggregated at the sample edges is removed with a razor blade. A mask aligner (*Karl Süss GmbH & Co. KG* MJB3) exposes the resist structure to a mercury lamp emission at $\lambda = 365 \text{ nm}$ for 6 s. Afterwards the development is performed in 1:5 dilution of developer

3.2. Sample Processing

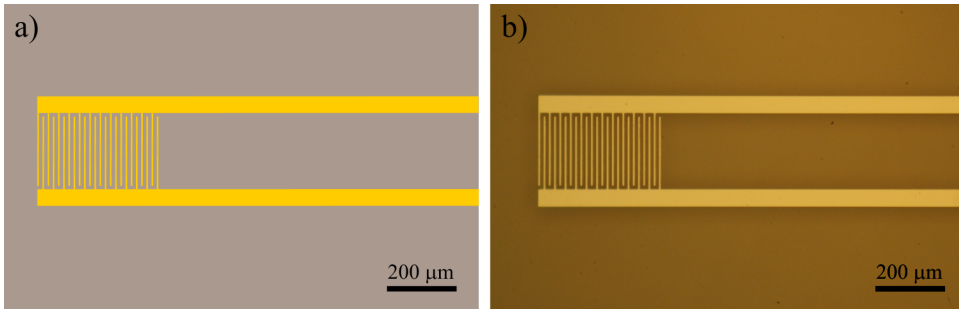


Figure 3.2.: Schematics (a) and microscope image (b) of sample O1 after the lift off process.

sample	contact materials	thickness (nm)	annealing
S1, O2	Ti, Au	20, 80	no annealing
O1	Ti, Al	10, 80	3 h at 510 °C in vacuum

Table 3.1.: Contact materials of the diamond samples.

(Rohm and Haas Company microposit Dev 351) and water, usually for 15 s.

Metal Contact Fabrication

Electron beam evaporation was used for attaching 20 nm of titanium and 80 nm of gold on oxygenated diamond surface for samples S1 and O2. Only for sample O1 contacts were evaporated thermally in a layer of 10 nm aluminum and 80 nm gold. After evaporation of the metal contacts lift off was performed in ultrasonic acetone bath at room temperature. For treatment steps of two minutes the ultrasonic power was increased in small steps. All used parameters are summed up in table 3.1.

Annealing of Contacts

Sample O2 was annealed after lift off for three hours at 510°C in vacuum. At this temperature aluminum diffuses into the gold and into the diamond surface decreasing the Schottky barrier height while mechanical stability is enhanced. Annealing was performed in a high vacuum oven providing a pressure below 3 nbar during the annealing process. Temperature was stabilized at a level of (510±10) °C.

3. Diamond Samples

Processing Metal Contacts on Diamond

A oxygen terminated surface allows the formation of an oxide at the surface, resulting in both an electrical contact and good mechanical stability of the thin metal contact. The influence of the selected material on the Schottky barrier height of contacts of high purity scds has been investigated during the 1990s. Titanium gold contacts on diamond are reported to exhibit Schottky barrier heights of about 1 eV on oxygen terminated surfaces Kawarada (1996).

Sample Cleaning

The standard cleaning procedure is rinsing the sample with acetone, then with isopropanol and final drying with nitrogen gas. In case of metal contamination a hot bath of sulfuric acid and potassium nitrate is used to remove base metal traces and organic residues. Diamonds are boiled in etching bath consisting of 20 ml H_2SO_4 and two spatula tips of KNO_3 at 225 °C for 60 min. Afterwards they are rinsed with deionised water.

3.3. Current-Voltage Characteristics

Three different samples are presented within the scope of this work. Small photocurrent ,typically in the range of pA, is measured with an trans impedance amplifier as described in 4.2. Samples are contacted with top gate electrodes processed as described in the previous section. Analysis of the current-voltage dependence allows for conclusions on conductivity and contact properties.

For determination of the dark current in the samples room light was switched off. Remaining diffuse light sources like instrument's displays lead to a difusive light intensity in the nW range, which was further reduced by additional coverage of the sample. Without photoionization only the reverse bias current can contribute to the dark current in Schottky diodes. Basically, thermionic emission allows electrons with high kinetic energy to tunnel into the contacts. Results of the current voltage characteristic measurements, conducted at room-temperature, are depicted in fig. 3.3. Very long settling times for the photocurrent were observed, indicating that the experiment was not in a dark state equilibrium. The relaxation time of the charge carriers and thus fermi level was reported to exceed hours for some diamond substrates with low carrier densities at room temperature, for varying illumination conditions Rohrer (1998). The recorded data of serves just as an

3.3. Current-Voltage Characteristics

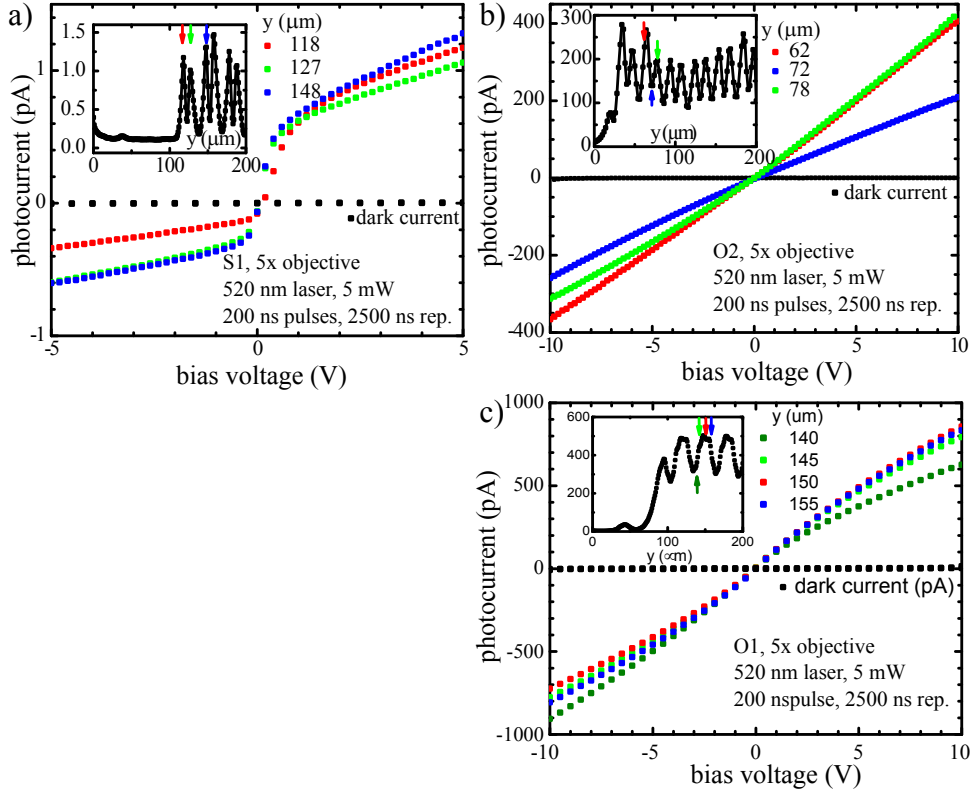


Figure 3.3.: *U-I* characteristics of photocurrent for the a) rectifying back to back diode sample S1. b), c) Samples O1 and O2 show a linear *U-I* dependence.

upper limit for the dark current *U-I* characteristic.

3.3.1. Photocurrent

A 5x objective illuminates homogeneously a diamond volume between several metal contacts. Photons separate charge carriers which are accelerated to the biased contacts. Results are shown in fig. 3.3.

For S1 a classical back to back diode characteristic is observed. Depending on the bias voltage sign either the first or the second Schottky contact is reverse biased, effectively limiting the total current. All three curves for S1 were taken on local maximums corresponding to different interdigital contacts, measurement positions are marked with arrows in the inset of a corresponding lateral scan across the contacts. Slope at origin and maximal

3. Diamond Samples

absolute amplitude vary as a function of the laser spot position relative to the contact and the contact quality itself. For constant contact properties throughout the contact structure and for a centered symmetric illumination a point symmetric shape is expected. The physics predicts the current to follow the law of the junction

$$I = I_s \left(\exp \left(\frac{qU_b}{nkT} \right) - 1 \right). \quad (3.1)$$

A saturation current I_s is expected for very high reverse bias voltage with $qU_b \gg nkT$. However such a saturation is not observed here, since even for $U_b > 1$ V still current increases significantly. For further analysis of this increase device geometry and the laser beam profile have to be taken into consideration, but this will not be discussed in the scope of this work.

Sample O1's U - I characteristic (fig. 3.3 b)) varies linearly in first approximation with U_b . A decrease in slope for $U_b < 5$ V could be attributed to effects of inhomogeneous illumination. Ohmic behavior is observed for sample O2 as well (fig. 3.3). Here, the illumination spot is broader, about 15 μm as can be estimated from the y -scan in the inset. Focusing only on one sign of U_b , a linear dependence with a slope related to the next positive contact's properties describes the data, as indicated in the by straight lines. To conclude, the U - I characteristic reveals the Schottky contact nature of sample S1 in contrast to approximately linear behavior of O1 and O2. The total current amplitude is about two to three orders of magnitude higher for the ohmic samples.

4. Experimental Setup for pEDMR and ODMR Detection of NV⁻ Centers in Diamond

The experimental setup will be described in this section. All elements of the entire experiment are mounted on an optical table, while most of the measurement equipment is located on a rack next to the table. Optical and microwave excitation can be controlled on a nanosecond timescale, while the implemented optical and electrical readout is averaging over hundreds of pulse sequences. The setup has been specially designed for NV⁻ center spectroscopy applications. It allows for nanometer resolution mapping of NV⁻ center photoluminescence and photocurrent. Based on these quantities sensitive to NV⁻ center population the underlying dynamical ionization and spin transition processes can be investigated. The setup with its three main components is depicted in fig. 4.1. The optics in the figure denoted with a), including details on the laser excitation as well as the detection of the specific NV⁻ center fluorescence is discussed in section 4.1. Another read out technique is shown in part b), where one detects photocurrent as a result of a two photon ionization of the NV⁻ center. Spin dynamics can be investigated when microwave interacts with the spin. Control parameters and details of the microwave circuit are discussed in section 4.2 along with the introduced electrical readout method.

4.1. Optics

4.1.1. Laser Sources

The optimal excitation wavelength for inducing NV⁻ center fluorescence is reported to be between 510 and 540 nm Aslam et al. (2013). In this setup a 520 nm solid state laser is chosen, which is in the middle of the interval. In total three different lasers were designed. The two other lasers beside the

4. Experimental Setup for pEDMR and ODMR Detection of NV⁻ Centers in Diamond

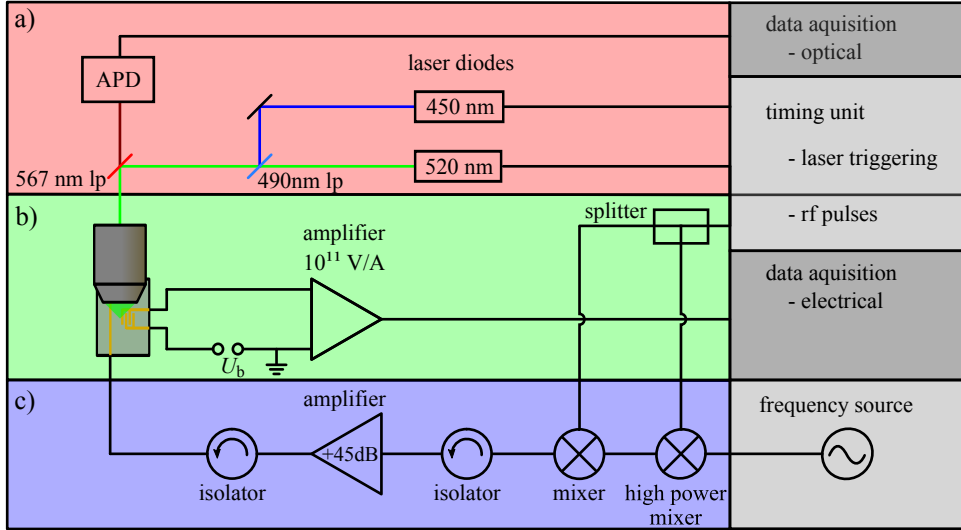


Figure 4.1.: a) NV⁻ centers are excited and ionized by pulsed laser illumination, while the fluorescent light caught in the microscope objective is guided to and detected by an APD. **b)** Photocurrent generated in the reverse biased MSM is converted into a voltage signal by a TIA. **c)** NV⁻ center spins can be driven coherently by microwave pulses provided by a massively amplified input signal originating from a frequency source.

green laser operate at wavelengths 450 nm and 785 nm, chosen for ionization of the NV⁰ center and NV⁻ center respectively. All lasers are self assembled systems, each based on a laser diode powered by a driver module. All laser components are depicted in fig. 4.2, while a more detailed overview of the laser diodes is given in table 4.1. For experiments with other lasers than those shown here the same optical principle can be used. For such a purpose appropriate matching of the reflection and transmission windows of beam splitters is required.

A nanosecond pulse driver module (*picolas* LDS-VRM-05) provides laser diode currents of up to 500 mA. It can be run in continuous wave (cw) mode or in pulsed mode, where the pulse width range can be increased dynamically from nanoseconds to arbitrarily long pulses. The laser driver itself only amplifies the input signal. A signal source sends the desired pulses of specific height and width to the *picolas* driver. In our case we use a 80 MHz waveform generator (*agilent* Agilent 33250A) producing pulses from 20-2000 ns with 5 ns rise time. The signal source is triggered by the experiment's timing control along with all other instruments like microwave

4.1. Optics

laser	λ (nm)	$\Delta\lambda$ (nm)	max. power (mW)	beam divergence ($^{\circ}$)
blue	450	2	80	11x25
green	520	2	50	7x22
NIR	785	not specified	90	9x16

Table 4.1.: Manufacturer's specification of the laser diodes.

source, positioning stage or detection systems. In section 4.3 the entire set of experimental steps is represented in the time domain for an exemplary pulse sequence.

An elliptical beam with specific aspect ratios for different lasers is the result of an aspherical lens in front of the laser diode. Here the desired numerical aspherical lens aperture is given by the diode's beam divergence. All aspherical lenses have anti-reflection coating appropriate for the corresponding wavelength regime in order to reduce laser intensity losses. For a precise positioning of the aspherical lenses mechanical stages with micrometer drives were used. Small variation of the diode lens distance allows for collimating the laser in a controlled way.

Although the laser power does not exceed the milliwatt range, the power consumption of the laser driver is not negligible. For cooling the laser driver base plate is mounted on an aluminum heat sink. In between the two metallic pieces a thin layer of thermal compound improves heat transport. A small fan below the radiator increases the effective air volume per time being available for cooling. Beyond the heat generated by the driver module the laser diode itself has to be considered as a heat source during lasing. When the laser diode is operated at high power it may heat up, due to limited heat transport through the diode pins. An additional path for heat transport is introduced by mounting the laser diode in a metal block with apertures for the diode pins and laser light, respectively. The metal block itself is screwed on the heat sink, separated only by an insulating mica foil and thermal compound.

The setup provides thermally stabilized lasers that can be driven at various pulse lengths, repetition rates and powers. All mentioned parameters can be controlled digitally within the experiment control program. Detailed information on the characteristics of the laser performances along with data of the laser suppression in the photon detection is provided in appendix ??.

4. Experimental Setup for pEDMR and ODMR Detection of NV⁻ Centers in Diamond

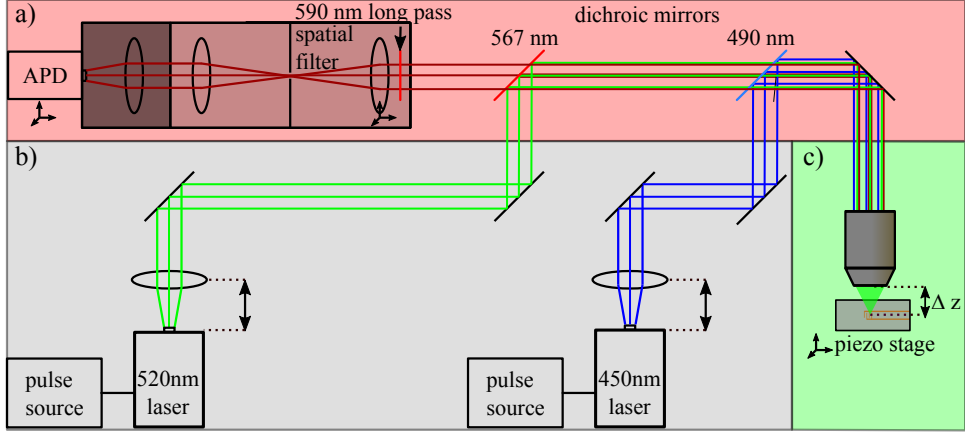


Figure 4.2.: a) The optical detection system transmits mostly light from NV⁻ while filtering out light from NV⁰ fluorescence the reflected laser light. Better depth resolution is achieved by implementing a spatial filter. b) A pulsed source signal is amplified by a laser driver module. The generated light is emitted into free space and collimated by a spherical lens to an elliptical laser beam. Position and direction of laser beams can be adjusted with two mirrors, whereas additional dichroic mirrors allow superposition of two lasers differing in wavelength. c) A microscope focuses the laser down to diffraction limit. Fluorescent light from this excitation spot is caught in the same objective and guided to the APD.

4.1.2. Confocal Microscopy

A confocal microscope composes an image of a sample exposed to light by scanning the surface. With the microscope objective in the right height above the sample both illumination of a small sample volume and collection of reflected or fluorescent light is possible. In general a beam splitter is necessary to couple a light source into the optical path from the objective to a photo detector. In this section a confocal microscope with two light sources, each coupled in with a corresponding beam splitter, is described.

Investigation of multiple photon excitation with different photon energy demands high accuracy in the laser alignment, because excitation and detection of the same sample volume has to be ensured. This section discusses details on the optics of the microscope in the setup, for which a schematic overview is given in fig. 4.2. The focus lies on the optical components required for confocal fluorescence microscopy for one or two laser excitation.

In fig. 4.2 b) the laser module is depicted next to the signal source. An

4.1. Optics

objective	magnification	NA	working distance (mm)	spot size (μm)
LMPLFLN100x	100	0.8	3.5	1.1 / 0.8
Plan-Neofluar 5x	5	0.15	22	6.0 / 23.1

Table 4.2.: Microscope objectives used in the NV spectrometer.

aspherical lens in front of the laser diode is positioned on an adjustable micrometer stage. When lens and stage are mounted parallel to the lasing axis defined by the laser diode, one can collimate the laser by moving the laser diode in the lens' focus. This is done by fine tuning the distance to obtain a constant laser spot size over a path of about two meters.

Two mirrors on kinetic mounts can be used to adjust the available degrees of freedom for a laser, position and direction. Precision screws on the mirrors allow for repeatable adjustments of the laser path. The third mirror is a dichroic long pass filter reflecting the laser light and transmitting fluorescent light to the APD. An additional mirror is mounted in such a way that it directs incident laser light parallel into the microscope objective. Depending on the inserted objective the focused laser spot occurs at a distance of 3.5mm or 22 mm. The sample is glued to a sampleholder which is mounted itself with isolated clamps on a piezo stage. In the large aperture of the piezo stage an objective can be inserted, either with 5x¹ or 100x² magnification. Details on the objectives are shown in table 4.2, spot sizes are given for both axial and lateral direction³.

Coarse positioning can be performed along the z -axis with a micrometer screw correcting the distance of the objective to the sample holder, as indicated in fig. 4.2 c). Feedback is provided by either the visible light being transmitted or reflected by the diamond, the NV⁻ center photoluminescence signal or the photocurrent signal. Fine tuning of the sample position is done with the piezo stage, this will be described in the following paragraph. It has to be stated however, that thermal long time fluctuations cause mechanical stress leading to misalignment over time in a self assembled optical setup with dimensions of meters.

Calibration of the detection mechanism can be achieved in the following way: First of all a glass cover slip or mirror is mounted above the objective

¹zeiss, Plan-Neofluar 5x/0.15 Ph 1, <https://goo.gl/hdCM1T>

²olympus, LMPLFLN100x, <https://goo.gl/3PqL1D>

³Diffraction limited lateral and axial spot sizes are calculated for a 520 nm laser using $d_{xy} = 0.61\lambda/NA$ and $d_z = \lambda/(NA)^2$.

4. Experimental Setup for pEDMR and ODMR Detection of NV⁻ Centers in Diamond

to generate a well defined reflection of the incident laser light. The rejected light gets collimated by the objective when the mirror is positioned in the focus plane. The laser reflex can be used to adjust the mirrors in order to superpose incident and reflected light, being an easily detectable phenomena indicating parallel beam paths. It has to be ensured that the laser illuminates the microscope objective's aperture. Further, by modulating slightly the focal distance Δz of the microscope objective and the sample, deviations from parallelism in the laser path occur as a xy shift of the laser reflex with respect to the incident laser path. The convention used throughout this thesis is that z corresponds to the direction of incident laser light propagation, whereas x and y span the plane perpendicular to the z -axis. Indeed the mentioned xy -shift can be observed visually on a screen with an aperture for the laser. While the spot shifts periodically with the modulation, the mirror system can be used to minimize the shift amplitude. The minimum of zero amplitude is reached when the laser beam path is parallel to the objective's axis.

4.1.3. Single Photon Avalanche Detector for NV⁻ Fluorescence detection

Silicon as detector material is a good choice for detection of the NV⁻ fluorescence, due to its sufficient photon detection efficiency in the spectral range from 400-1000 nm. We use a single photon avalanche detector (*ex-cellitas* SPCM-AQRH-10), with a photon detection efficiency η meeting the requirements: In the main part of the NV⁻ fluorescence from 600-800 nm, η is above 60%, but also further utilization might be considered when photon detection in the interval of 400-1000 nm is required ($\eta > 10\%$). When it comes to detection of single photons not only a high quantum efficiency but also detector dead times and dark counts become important. The APD is specified to perform at a dark count rate below 1500 counts per second (cps), however we determine the real value to be 600 cps. With a dead time of $\tau_d = 22$ ns after detection of a photon a rough estimate for the maximal count-rate yields $1/\tau_d \approx 45$ Mcps. And indeed, the manufacturer specifies the maximum count-rate before saturation to be 37 Mcps, close to the estimate. To describe correctly the dependence on incident count rate and measured value a correction factor is introduced. Linear behavior is guaranteed at count-rates below 1 Mcps, while correction factors of >1.4 above 10 Mcps have to be taken into account. Time resolved data acquisition could be possible using a fast read out device, allowing for detection of the decay times on a ns timescale.

4.2. Electronics

For the alignment of the optical detector path the same reflected laser light may be used. The detection system as shown in fig. 4.2 a) consists of a band pass filter, spatial filter and a focusing lens in front of the detector chip. All mentioned components are protected from room ambient light by a black casing. Light passing the objective in reverse direction transmits the long pass filters and enters the casing through an aperture of about 10 mm. There an additional filter, a long pass filter absorbing below 590 nm, suppresses remaining laser reflections and NV^0 fluorescence. It is mounted together with a planoconvex lens on a *xyz* stage. A spatial filter, a set of two lenses and a pin hole in the lens foci, selects one plane for transmission. Light from other sources is not focused on the pinhole, which results in massive light suppression behind the pinhole. The components used are a planoconvex lens (*thorlabs*, $f=150$ mm), a 100 μm pinhole (*thorlabs*, P100S) and a collimating planoconvex lens after the pinhole (*thorlabs*, $f=75$ mm). Finally another lens ($f=40$ mm) projects the pinhole on the detector chip, where the fine positioning is enabled by a *xyz*-stage of the APD. Within the optical alignment it was ensured that lenses are mounted perpendicular to the light path. To observe this experimentally the 590 nm long pass filter was removed, resulting in a sufficient intensity of laser light being reflected from a glass cover slip. On this well defined axis the entire photo detection system was aligned. Special care was taken of mounting the lenses along the z -axis by centering lens reflections on the incident light path. Once lenses and pinhole were mounted, the pin hole was brought into focus by manually fine tuning the distance. Finally, for the detector positioning step incident light intensity was reduced with a optical density (OD) filter to prevent damage due to excessive light exposure.

After this aligning process a spectrometer calibration is recommended for a quantification of the laser suppression and dark counts. An exemplary data set is shown in appendix ??

In conclusion the used APD meets the requirements of detecting NV^- fluorescence counting individual photons. Combined with a spatial and a long pass filter a small fluorescing volume in the sample can be investigated.

4.2. Electronics

4.2.1. Low Noise Transimpedance Amplifier for Photocurrent Detection

The level of pohotocurrent is mainly dependent on

4. Experimental Setup for pEDMR and ODMR Detection of NV⁻ Centers in Diamond

- density of NV centers
- illumination intensity
- bias voltage
- repetition rate and
- photoconductive gain

as discussed in more detail in section ?? . However, we end up under typical experimental conditions with current levels in the pA regime, when the sample is reverse biased. If not stated otherwise, the bias voltage is 5 V, provided by a stable voltage source (*Yokogawa GS200*). Under illumination a pA photocurrent is now generated. A low noise transimpedance amplifier (TIA) (*femto DDPICA 300*) is capable of realizing amplifications up to 10^{11} V/A at a bandwidth of 20Hz and up to 10^{13} V/A in slower operation modes. The amplified signal at the TIA output is read out by a multimeter (*Keithley 2000*, 6 1/2 digits). Optimizing parameters for the readout considering a measurement delay corresponding to the TIA rise time and the integration time allows low noise current detection comparable to the TIA specifications⁴.

4.2.2. Microwave Circuit

Electron spin resonance in the NV⁻ center is performed with strong mw pulses applied on a gold wire in close vicinity of the illuminated sample volume. An initial rectangular pulse is split equally in two parts by a power splitter (*minicircuits ZAPD-4+*), as shown in 4.1 c). One pulse fraction is mixed with a carrier frequency of 2-3 GHz in a frequency mixer (*minicircuits ZX05-43-H+-ST*). The local oscillator input is fed by a frequency source (*agilent E8257D*) signal of 13dBm. Subsequently a second frequency mixer (*minicircuits ZX05-43-H+-ST*) optimizes the mw pulse shape by multiplying it with the initial pulse. Both frequency mixers are passive elements,

⁴spectral input noise density of $1.3\text{fA}/\sqrt{\text{Hz}}$ for $10^{10} - 10^{11}$ V/A and $0.2\text{fA}/\sqrt{\text{Hz}}$ for the $10^{12} - 10^{13}$ V/A amplification regime.

4.3. Timing Control

absorbing a fraction of the input power, typically 6 dB. After the desired mw pulse has been composed in the frequency domain it is amplified to a microwave power of 10 W. For sample S1 the microwave power at the gold wire was determined to be 9 W with a fast microwave diode. For O1 and O2 a microwave power of 14 W and 11 W was recorded. The rf amplifier (*minicircuits* ZHL-16W-43+, typ. gain +45 dB) is isolated with circulators to reduce reflections. One circulator (*mcli* IS-10-1) reduces internal amplifier reflections passing the input port, otherwise perturbing the mw mixing, whereas the second circulator (*mcli* IS-10-10) protects the amplifier output from reflections at the sample. The microwave interface at the sampleholder is given by sma-connectors. Finally, the microwave terminates in a 50Ω resistor at the end of the sampleholder's transmission line which absorbs most of the mw power.

Analysis of the power levels at the mw components would reveal the following: The initial local oscillator signal of 13 dBm gets mixed with the rectangular pulse at the rf port, resulting in a mw output power of 7 dBm because it is attenuated in the first mixer by 6 dB. Taking the splitter loss into account, one should consider that both pulses after the splitter are at -3 dB. After the second mixer the pulse power is about 1 dBm. Considering both circulators also as damping elements one ends up with a +45dBm amplification of rf pulses to powers of 45 dBm, or 30 mW. This relates to a rf power of 10-20 mW, as determined by an independent measurement with a mw diode.

4.3. Timing Control

Operating coherently with an ensemble of quantum states requires precise control of the excitation. To obtain a better understanding of the underlying dynamic processes an experiment requires a time resolution better than the time constants given by the system under study. For the NV⁻ center in diamond it is known that spin dependent lifetime of the optically excited state is 13 ns for the triplet state or 77 ns for the singlet state, as explained in section ???. It is obvious that any experiment allowing for a study of the dynamics in the NV⁻ center has to operate on a timescale comparable to the lifetime of states. Further it turns out in theory and experiment that singlet triplet transition rabi times τ_R under the given microwave powers are in the order of 100 ns. Optimization of microwave pulses makes only sense, when the length can be varied by few percentages of τ_R . The choice of a pulse card with a 500 MHz clock meets the mentioned requirements, both for

4. Experimental Setup for pEDMR and ODMR Detection of NV⁻ Centers in Diamond

optical induced electron transitions and microwave induced transitions of the spin system. On multiple channels pulses of variable length and spacing can be programmed with 2 ns resolution. The following section 4.3.1 describes how the excitation pulses evolve within the setup, whereas section ?? gives a more detailed view on the experiment as an interplay of the piezo-positioning system, the pulsed excitation and simultaneous measurement.

4.3.1. Excitation Pulse Sequence

The pulse card (*spintronics* PBESR-PRO-500) is capable of producing pulses as short as 12 ns with a 2ns resolution. The time resolution is a consequence of the clock frequency of 500MHz, while the shortest pulse duration is given by internal electrical circuitry. Typically one pulse p_{MW} restricting the length of the microwave pulse and a second pulse acting as trigger for the laser signal source are launched with adjustable reference time. How these pulses evolve during the experiment is illustrated schematically in fig 4.3. A first mixer composes a signal from the frequency source with a 50% fraction of p_{MW} . A second mixer optimized for lower powers again mixes the resulting signal with the other part of the initial rectangular pulse, effectively reducing undesired high frequency artifacts stemming from deviations from a perfectly rectangular p_{MW} , as shown schematically in fig. 4.3 b). The strong excitation mw field is generated by a subsequent amplification. In fig. 4.3 c) the laser pulse generation with respect to the control pulse is depicted. An initial TTL pulse is released by the pulse card triggering the signal source to perform a rectangular pulse of required length and amplitude. At next the laser driver translates this signal into a laser pulse, details of this conversion are discussed in appendix ??.

The pulse card generates pulses on up to 24 distinct outputs, where currently the first three are assigned to lasers and the fourth to the microwave circuit. In the control program the required parameters for the timing unit can be set arbitrarily in the limits of 2 ns resolution and a minimal pulse length or pulse delay of 12 ns, spacing of pulses requires a definition of a reference time. Available reference points may be chosen at the end or start of the subsequent pulse. It might be necessary to check pulse delay differences directly at the sample caused by different cable lengths or instrument reaction times, especially when small time delays of several ns play a non negligible role.

4.3. Timing Control

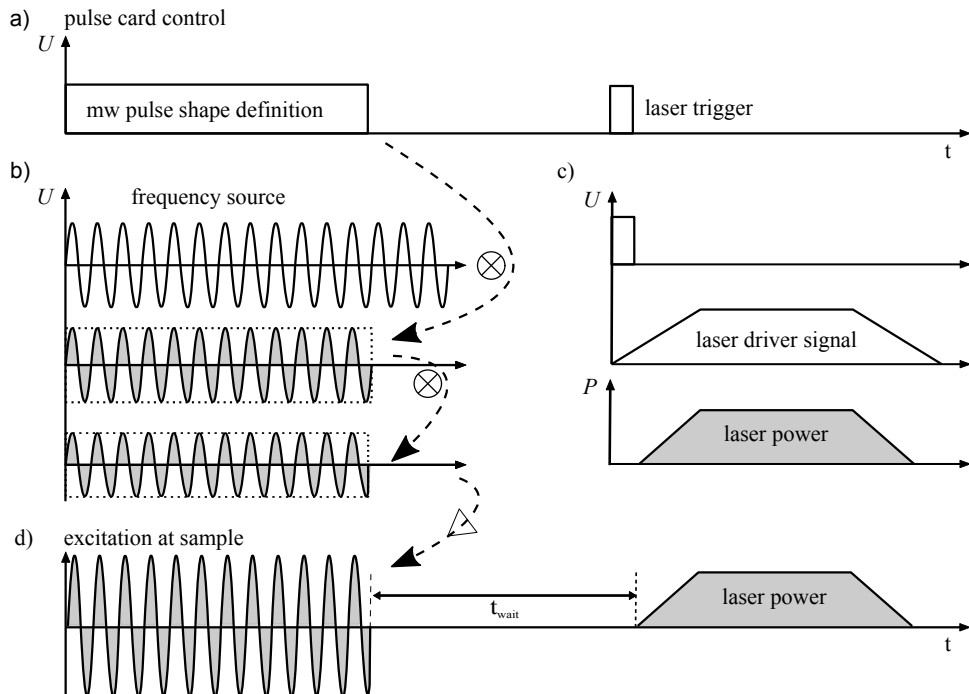


Figure 4.3.: A pulse card coordinates the optical and microwave excitation of NV⁻ centers. a) A control pulse defining the width of the microwave excitation and a laser trigger pulse are generated. b) Composition of the microwave pulse by mixing twice p_{mw} with the desired frequency. c) Additionally a pulsed signal source triggered by another control pulse operates the the laser driver. d) Both the length of the pulse sequence and the reference times between pulses can be adjusted as required.

5. Basic Experiments

In this chapter the experimental investigation of the NV⁻ center is presented. First of all the optical excitation with laser light and optical detection is presented and how the device performs under laboratory conditions. Two detection techniques, electrical and optical detection of magnetic resonance (EDMR and ODMR, respectively) are presented separately, to be used interchangeably later on. When the basic signal generation principles are understood the experiment can be extended to study spin microwave interactions in detail (sections 5.1.2 and 5.3). Characteristic experiments demonstrating spin control are shown in section 5.3 including a discussion of electrically and optically detected magnetic resonance results. Improvement of spin contrast is conducted by investigating the dynamics of NV⁻ center ionization in section 6.

5.1. Photoluminescence Detection and ODMR of NV⁻ centers

The photoluminescence strongly varies with the choice of the microscope objective. The benefit of high spatial resolution and high optical power can be realized with the 100x objective, a much more homogeneous illumination in the detection volume is achieved when the 5x objective is used. Depending on the application the objective meeting the requirements best is chosen. First the resolution of laser excitation and the detection method will be discussed in sections 5.1.1 and 5.2.3. With this background information on the illumination conditions ODMR results can be interpreted better (section 5.1.2).

5.1.1. Spatial Resolution of the Photoluminescence Detection

The maximal resolution utilizing the objective with 100x magnification can be achieved when the sample surface is brought into focus. Strong 520 nm laser pulses of 50 mW ionize the NV⁻ centers in a two photon absorption process. The incident elliptical laser beam is focused down to a spot limited

5. Basic Experiments

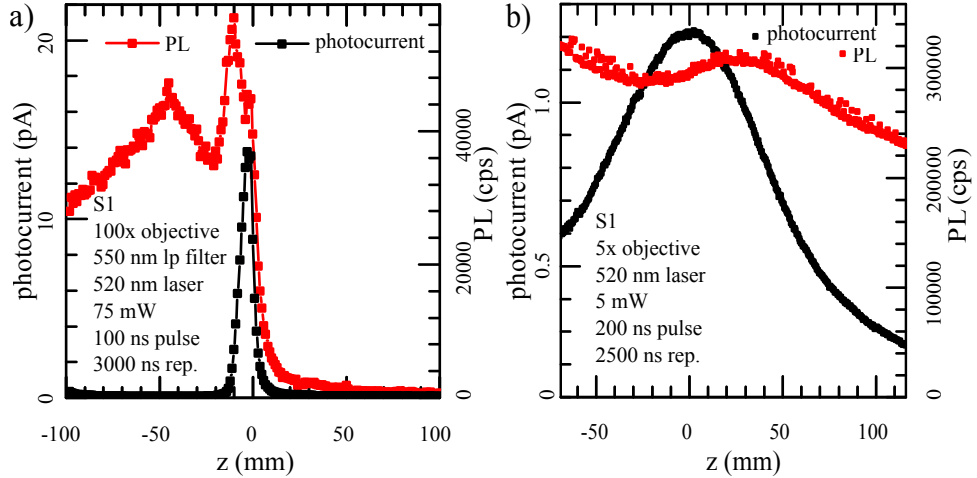


Figure 5.1.: a) When the diamond surface is brought in focus a steep increase in photocurrent (black data points) is observed. Carrier transport is optimal close to the surface resulting in a decrease as the laser penetrates the sample. The situation is different for the photoluminescence (red), where photons emitted by excited NV^- centers penetrate the transparent sample regardless of the excitation depth. b) Homogeneous illumination of a small sample volume with a 5x objective. A lower spatial resolution is the trade-off.

by the width of the point spread function (PSF), which is determined by the beam profile and the objective's NA . The resulting signal as it is measured by the optical detection system is the convolution integral of the light profile with the laser intensity dependent photoluminescence and the spatial transmittance of the detection system. Only photoluminescence photons emitted in the excitation plane are projected on the detector chip as a consequence of the spatial filter selection. Exemplary data for a high resolution scan in axial direction is shown in fig.5.1 a.

In the data set the z -axis origin is set to the sample surface. As the laser spot penetrates the surface the photocurrent increase is maximal. This is in fairly good approximation where the photocurrent is at a fraction of its maximal value. Within the scope of this work the z -origin is assigned to the position where the photocurrent is at 20 % of its maximal value. For the 5x objective the situation is different, since the laser spot length is not any longer smaller than the conductive surface region. Then the surface is assigned to the photocurrent maximum. Generally positive z represents in the distance of the laser spot center above the diamond surface, negative

5.1. Photoluminescence Detection and ODMR of NV⁻ centers

z the penetration depth. Theoretically a diffraction limited spot diameter of $1.1 \mu\text{m}$ is expected for a Gaussian beam profile. However, for positive z larger than this value still small PL intensity is detected due to an out-smearing of the focused laser spot. This effect increases with larger, non Gaussian beam diameter and thus also increases for elliptical beams with aspect ratio >1 . When the spot hits exactly the surface signal is maximal, most probably because some of imperfect suppression of reflected laser light. A more or less constant PL intensity is observed in the sample volume, being in good agreement with an uniformly nitrogen doped diamond sample with homogeneous NV⁻ center concentration. Remaining z dependencies can be attributed to shading of fluorescent diamond material by metallic contacts, as the diameter of illuminated surface reaches the contact gap size. Another aspect that has to be considered here as well as for the discussion of photocurrent laser on is the misalignment of the optical axis and the surface normal vector. The optical axis is well defined through the adjustment process to be in parallel with the optical table's translation stages and the objective. The sampleholder is mounted mechanically under strain on the stage and can not guarantee for sample surface orientation perpendicular to z . One consequence is that lateral coordinates defined by the sample, i.e. metal contact edges, shift with z . A second effect is that one has to ensure to measure at the same height above the sample surface when measuring at different lateral positions.

When homogeneous illumination is required, a laser spot of dimensions larger than the volume of interest has to be generated. Photocurrent can only be detected close to the surface, as long as it not generated deeper than $10\text{-}20 \mu\text{m}$. With a $5\times$ objective a laser spot size of $150 \mu\text{m}$ axial length is created, in good approximation illuminating homogeneously the uppermost conductive diamond layer. The photoluminescence data in fig.5.1 b shows a pronounced first maximum at the surface, followed by a decrease in a depth of about $40 \mu\text{m}$ and rising to the original maximum value for $z = 100 \mu\text{m}$. The variation can be explained by shading of illuminated volume by a single metal contact.

5.1.2. ODMR on NV⁻ centers

The spin of the NV⁻ center can be addressed with microwave pulses. Here, investigation of the photoluminescence as a function of microwave frequency, commonly called an ODMR experiment, will be discussed as a read-out technique. It is known, that spin polarization of NV⁻ centers can reach 80 % under cw laser excitation even at room temperature Acosta et al. (2010b). To study spin dynamics pulsed laser and microwave sequences are used,

5. Basic Experiments

where the APD integrates photoluminescence over many cycles. Rectangular microwave pulses of variable frequency are used to manipulate the spin by inducing transitions from the ground state singlet $|1\rangle$ to the triplet $|2\rangle$, expressed in the nomenclature of section 2.1.2. The photoluminescence change induced by spin preparation before laser excitation will be discussed in this section. In absence of microwaves electrons get excited and relax into the NV^- ground state, symbolically written as $|1\rangle \rightleftharpoons |3\rangle$. The non-radiative relaxation into the dark state, $|3\rangle \rightarrow |5\rangle$, can be neglected since the partial lifetime $\tau_{31} \ll \tau_{35}$. When the NV^- spin is initialized into $|2\rangle$ the excited electron undergoes the laser induced transition $|2\rangle \rightleftharpoons |4\rangle$. Non-radiative relaxation is here important, since the transition rate to the dark state is comparable to the radiative decay rate, $\tau_{42} \approx \tau_{45}$. The resulting population of $|4\rangle$ is lowered by the fraction of electrons being stored in the dark state, which is close to zero for initial state $|1\rangle$ and significantly large for initial state $|2\rangle$. Subsequent photo-ionization proportional to population of states promotes fewer electrons to the conduction band for the ladder case, which means less photocurrent. The expected drop of photocurrent attributed to spin manipulation on the initial NV^- center ground state can be measured experimentally, as presented in fig.5.2 a.

Photoluminescence is measured during a continuously repeated pulse sequence. A 50 ns microwave pulse of 9 W acts on all NV^- centers in the sample. Due to different strength of the radially decreasing electromagnetic field spin transition efficiency varies with the distance from the microwave wire. Depending on duration, strength and frequency of the interaction with the electromagnetic field forms a superposition of states $|1\rangle$ and $|2\rangle$. A strong 520 nm laser pulse of 100 ns duration excites a diamond volume in focus of the high magnification objective. The laser excitation is delayed by 100-200 ns with respect to the end of the microwave excitation pulse to ensure well defined experimental conditions. Spin coherence outlasts this delay by far since both spin coherence and relaxation times are much longer than this delay. Spin coherence time depends strongly on nuclear and paramagnetic impurities, where ^{13}C is the dominant decoherence source in type II diamonds Stanwix et al. (2010). Ensemble NV^- spin coherence times exceeding hundreds of μs even at room temperature have been reported for comparable type II diamonds substrates. The signature of the NV^- center spins undergoing transitions into $|2\rangle$ can be seen in the experimental data as a signal reduction at frequency 2.87 GHz, where the photon energy $E_{\text{ph}} = hf$ matches the zero field splitting parameter $D = 0.012$ meV. As used in the following section 5.2 the signal reduction, always measured relative to the off-resonant total amplitude, is called contrast. The signal to noise ratio of 20:1 can be

5.1. Photoluminescence Detection and ODMR of NV⁻ centers

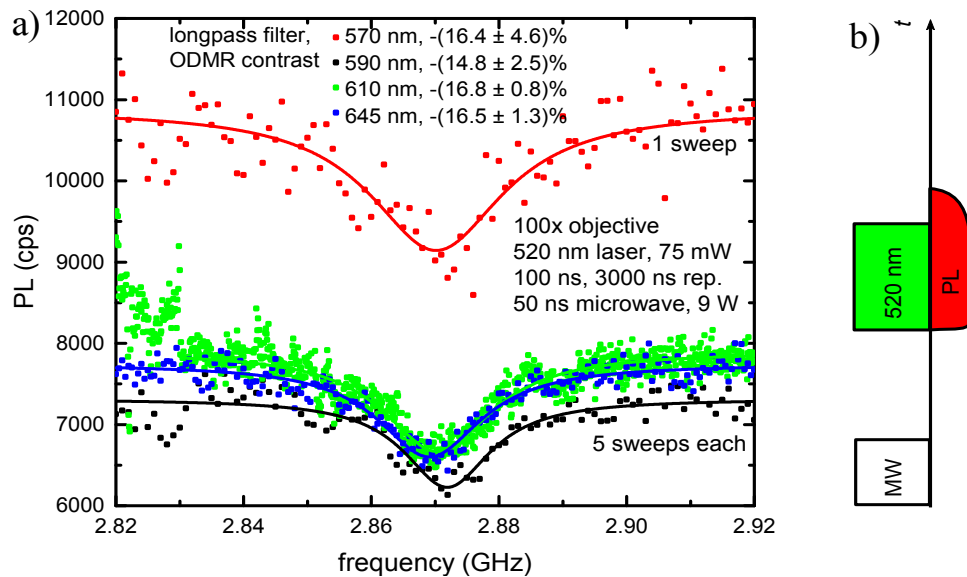


Figure 5.2.: a) Under green laser illumination microwave driven spin transitions lead to population of the non-fluorescent dark state, detectable as a decrease of PL. ODMR data measured using different filters in the APD detection system. Solid lines are Lorentzian fits to the data. For the 610 nm filter measurement the first off-resonance data points were recorded with the laser in a cold state and therefore excluded from the fit starting at 2.83 GHz. This signature did not reappear in sweeps 2-5, indicating a switch-on effect. **b)** The applied pulse sequence is shown schematically, not to scale in time or intensity.

5. Basic Experiments

improved by increasing the photon count rate and waiting for the laser to stabilize after switch on. A Lorentzian is fitted to the data describing an absorptive process. From the fit the parameters linewidth, resonance frequency and amplitude of the resonance can be obtained, yielding an ODMR contrast of $-(15 \pm 2)\%$. This experiment was repeated with different PL filters in order to find optimal experimental conditions providing maximal spin contrast.

Selecting an Appropriate PL Filter

If there were other photoluminescent sources than NV⁻ centers longpass filters are the instrument of choice for reduction of PL that is not attributed to the NV⁻ center. One would expect a cutoff wavelength close to the NV⁻ ZPL to show best performance. The very same ODMR experiment from above was conducted after changing the longpass filter in the photo detection system to different ones with cutoff wavelength at 590 nm, 610 nm and 645 nm, respectively. The optical path was readjusted after every filter change to exactly map the excitation spot to the detector. Experimental results are shown in fig.5.2 a.

A major difference is the difference in total signal amplitude, being at a similar level for all filters but the 570 nm filter. This can be attributed to a weak suppression of reflected laser light by this filter. Since laser reflection is not influenced by the microwave field it just gives a constant contribution to the PL signal. Without the reflection offset, that can be suppressed with other filters, ODMR contrast is theoretically higher. In an independent experiment the suppression quality of the detector system with the 590 nm longpass filter has been characterized. The intensity of 520 nm laser light reflected from a mirror was measured with the APD system for different incident laser powers (appendix A.3). From these measurements can be concluded, that still laser light enters the detection system, but an upper limit of this parasitic effect can be evaluated.

Taking a closer look at the noise level reveals highest fluctuation for the 570 nm data set. The other curves are the normalized result of five similar f -sweeps conducted in sequence. Lorentzian fits provide the area of the resonance and line width, from that the contrast can be derived. The independent errors of line width and dip area determine the contrast errors according to the rules of error calculation. We note the small shifts of about 1 MHz from resonance frequency 2.871 GHz within in the data sets, that can be explained by uncertainties originating from the low signal to noise ratio in this measurement. For data analysis the comparably low dark-count

5.2. Photocurrent Detection

rate of 600 cps was not subtracted. Within the error bars contrasts of all data sets coincide with an ODMR contrast of 16%. Without any significant difference between filters 590, 610 and 645 nm we decide for 590 nm, because its relatively low cutoff wavelength provides full transmission of the NV⁻ PL spectrum.

5.2. Photocurrent Detection

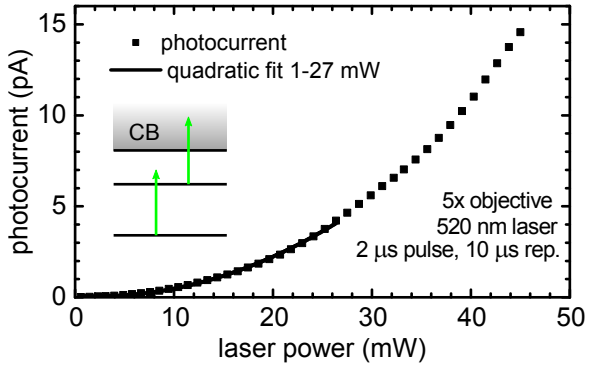
So far we focused on the PL signal for detecting the spin resonance. In this section the pEDMR method will be explained and demonstrated in detail. The first aspect is finding the right power range for pEDMR, then spin transition experiments will be shown. Even in absence of external magnetic field the NV⁻ center spin is orientated along a local atomic magnetic field along the defect axis. With this magnetic field as prerequisite for Rabi experiments spin transitions in a two level system can be induced (section 5.3.1). Having learned about the microwave spin initialization further insight into photocurrent dynamics is obtained from detailed study of laser excitation time and intensity. Optimal spin contrast is obtained for a laser pulse length that relates to internal transition times of the NV⁻ center.

5.2.1. Two Photon Ionization of NV⁻ center

For photoionization in diamond more than one visible photon is required. In the model introduced in section ?? a four photon process is described for green laser light. Experimentally access to this multiple particle excitation gives analysis of laser power dependent photoionization. Basically a rate equation system including all, power dependent, NV⁻ center related transitions has to be solved. In a very simplistic view the exponent of the power dependence equals the amount of photons involved, but this is no longer valid for saturation effects. If population inversion occurs, higher laser power does not result in more photo excitation since there are no more electrons available for excitation. The experiment was conducted on sample S1 under homogeneous laser illumination with the 5x objective. The main feature in the data observed, shown in fig.5.3, is a quadratic laser power dependence of photocurrent. Two transitions determine the observed quadratic relation, transition $|1\rangle, |2\rangle \rightarrow |3\rangle, |4\rangle$ from NV⁻ ground state to its excited state and subsequent $|3\rangle, |4\rangle \rightarrow \text{CB}$. Recharging, NV⁰ to NV⁻ conversion, by photoexcitation of NV center states in the valence band takes place on a timescale much faster than NV⁻ center ionization. The dark state does not provide a

5. Basic Experiments

Figure 5.3: Quadratic dependence of the photocurrent for a two photon ionization process of the NV⁻ center. For laser powers above 100 mW the first transition saturates and the power dependence is expected to become linear Hrubesch et al. (2017).



concurring ionization path and can be interpreted as a reservoir for a very small fraction of electrons that do not relax into the triplet ground state manifold. From the dark state electrons relax through another dark state level back into the ground state. The relaxation process from the dark state into $|1\rangle$ or $|2\rangle$ can be described by two time constants, 289 ns and 463 ns respectively Hrubesch et al. (2017). The photoionization experiment should be ideally conducted under cw laser illumination. Since pumping power is higher in pulsed mode we choose as trade-off a pulse length of 2 μ s, an order of magnitude higher than any dominant relaxation time of the NV⁻ center. At low laser power photocurrent linear contribution from N_s⁰ photoionization competes with the quadratic two photon ionization contribution of NV⁻ centers, as reported by Bourgeois et al. (2015). In our experiment a linear contribution is not significant, due to dominating measurement uncertainties at low photocurrent levels. With increasing laser power N_s⁰ ionization is outperformed by NV⁻ ionization. At some threshold power population inversion of singlet ground state and excited state occurs. Further linear photocurrent increase is expected and experimentally demonstrated to occur for laser powers above 80 mW using a 5x objective (NA 0.15) Hrubesch et al. (2017). The quadratic fit does not include data points above 27 mW to be independent of population inversion effects at higher powers. In section ?? will be analyzed which pumping power is suitable for efficient electrical NV⁻ spin read-out.

5.2.2. Characteristics of the MSM Photodetector

Typically a bias voltage of $U_b = 5$ V is sufficient to accelerate the charge carriers separated by photoionization. The chosen U_b corresponds to an average electric field of $E = 5 \cdot 10^3$ V/cm in the 10 μ m gap between con-

5.2. Photocurrent Detection

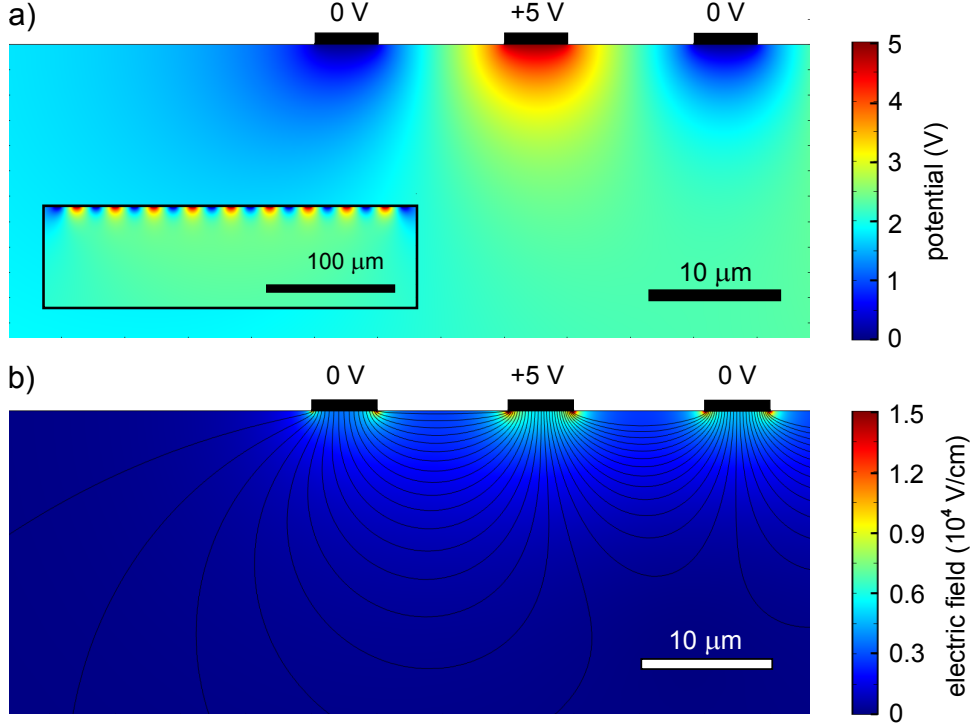


Figure 5.4.: a) Simulation of electrostatic potential for the MSM device under 5 V bias voltage. The gap between contacts is 10 μm , the contacts are 5 μm broad and 0.1 μm thick. The inset depicts the potential periodicity of 30 μm . b) Electrical field is maximal in the vicinity of contacts, field-lines are illustrated as black lines and the corresponding magnitude is encoded in the background color. For carriers deeper than 15 μm collection efficiency is low.

tacts. The electric potential of an exemplary interdigital contact structure is simulated with isolated top gate electrodes on a material with dielectric constant of diamond. The problem can be described in two dimensions for a contact length being much larger than width and spacing. The result for the simulated electrostatic potential is illustrated in fig. 5.4 a).

The only 100 nm thin contacts are depicted as black bars for better visibility. Every second contact is connected to U_b , all others are grounded. In detail shown is the region close to the fist contact and how potential becomes nearly homogeneous 20 μm away from the contacts, which is twice the contact spacing. This homogeneity is a first indication for a depth dependent limit

5. Basic Experiments

in carrier collection efficiency. The inset depicts a very regular pattern for all simulated contacts that occurs close to the surface. The periodicity of $30 \mu\text{m} = 2 \cdot (10\mu\text{m} + 5\mu\text{m})$ relates to that of the contact structure, when only every second, positively biased, contact is counted.

Figure 5.4 b shows the corresponding electric field distribution for the MSM detector. Maximal field occurs at the contact edges where curvature is maximal. At the very first contact a smaller electric field can be followed from both the blurring and the lower potential difference to the unconnected area. Indeed the high field area at the first contact at $y=0$ is reduced compared to the inner contacts. Within a depth of one micrometer there is no significant change in potential and field distribution for the active, illuminated detector volume. For deeper regions, $-1 \mu\text{m} > z > -5 \mu\text{m}$, carriers have to take increasingly longer paths along the electric field lines to the contacts. Increased path length along with reduced electric field amplitude reduces the carrier detection efficiency. For $z = 7 \mu\text{m}$ the path length is twice that of a near-surface path. We can compare this value with the result of the depth dependent scan of photocurrent with a FWHM of $8 \mu\text{m}$. This match confirms the argumentation from above. To conclude, the self-assembled MSM photodetector detects charge carriers generated in an active volume close to the surface. Together with the picture of low field mobility transport (section refsec:basics:MSM detector) the device working principle is well understood.

5.2.3. Mapping the photocurrent

With background knowledge on MSM detector performance and the underlying photocurrent generation process the lateral dependence of the signal will be discussed. As it will turn out it is not uniform at the surface, but the observed variations allow to select a detection volume with high signal output. Further, conclusions on the lateral resolution and the laser spot size can be drawn. Detailed diamond surface scans with the 100x objective yield data like that depicted in fig. 5.5 a.

The most prominent feature in this non-linear graphical representation are the black and white areas indicating positions of metal contacts and active detection volume. The interdigital contacts occur under an angle of 38° with respect to the scan direction. In all experiments we assign the y -axis perpendicular to the contacts, as indicated in the figure. The x -axis completes the system of y -axis and the surface normal z -axis to a right handed coordinate system. The data trace along the depicted line (fig.5.5 b begins at zero photocurrent at the edge of the MSM structure and continues with a regular data structure beginning at $y=30 \mu\text{m}$. As we would have expected from the

5.2. Photocurrent Detection

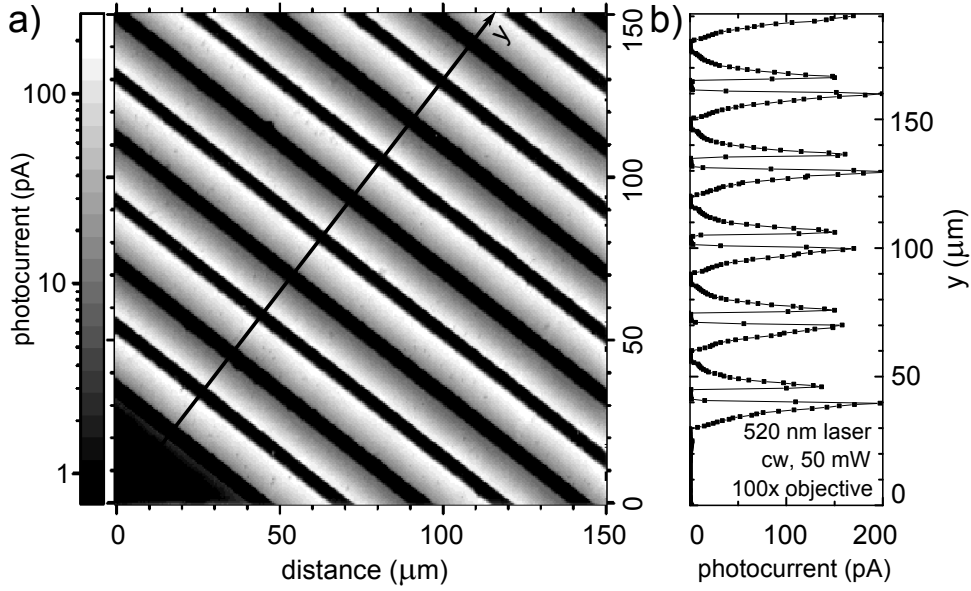


Figure 5.5.: a) A surface scan while photocurrent is measured reveals the position of metal contacts, visible as black stripes. For better contrast a logarithmic scale is chosen in the image. In the bottom left corner charge carriers cannot be detected in absence of contacts. Data of a slice perpendicular to the contacts is shown in b). Alternating bias voltages at the contact lead to suppressed or enhanced detection of the photo-ionized carriers.

electric potential simulation indeed a regular pattern with $30 \mu\text{m}$ periodicity can be observed and the contacts with $U_b = +5V$ identified, the first one at $40\text{-}45 \mu\text{m}$. Looking carefully to the first grounded contact at $y = 25\text{-}30 \mu\text{m}$ brings a very small photocurrent for $y < 25 \mu\text{m}$ to our focus, better visible in the logarithmic image representation. Since this is one low potential contact not electrons but holes contribute dominantly to the photocurrent. The field distribution here is very different from the homogeneous one in the area between contacts, decreasing approximately radially at this outer edge. In any gap between contacts there is maximal photocurrent detected at the positively biased side. At the first sight this is contradictory to the electric field symmetry. The interpretation here is that both holes as electrons get collected with the same efficiency close to the corresponding contact with highest efficiency, but ladder result in a photocurrent that is enhanced by the photoconductive gain factor.

Another parameter that can be analyzed is the flank slope at the positive

5. Basic Experiments

contacts. It is the convolution integral of the laser spot point spread function (PSF), the NV⁻ density and the space dependent efficiency of the MSM detector. The NV⁻ density is homogeneous throughout the sample but some regions shaded by the contacts must not contribute to the integral. Under the assumption of a step function modulating the NV⁻ density and a constant efficiency close to the contact the lateral laser PSF can be measured. For a gaussian beam profile the flank slope can be determined analytically to be However, since the photocurrent depends quadratically on the laser power and thus the PSF, we have only experimental access to the squared PSF, which is sharper. To introduce an easily accessible quantity one can determine the 10 % - 90 % width above a contact as estimate for the spot size. From the data of fig. 5.5 we measure $(1 \pm 0.3) \mu\text{m}$ at the sharp flanks. Further the other broader flanks can be analyzed allowing for conclusions on the MSM detection efficiency. It cannot be determined with higher precision than the spot size. The efficiency seems to decrease somehow reciprocal with the contact distance, detailed analysis and comparison with the field simulation have to be conducted. Another remarkable feature is a reduced height and FWHM at the contact side with higher y . This asymmetry is introduced by the laser beam, that was not perfectly aligned with the sample surface vector. However, quantitative characterization of this effect assuming a angle mismatch of 1:100, roughly the experimental accuracy, could explain the observed differences of about 20% when not only to linear geometric effects such as shading but also non-linear electric field dependencies are taken into consideration. This will not be discussed in the scope of this work. We just state that the angle of incidence has a strong effect on the maximal photocurrent amplitude.

5.3. Pulsed Electrical Detected Magnetic Resonance on NV⁻ Centers

Knowing about the photocurrent generation, a four photon excitation process under 520 nm laser illumination, photocurrent change induced by variation of electron and spin excitation will be analyzed in this chapter. This read-out method is commonly referred to as pulsed Electrical Detected Magnetic Resonance (pEDMR). Again, a small averaged pA photocurrent generated by a continuously repeated pulse sequence is the measurement signal. Conditions for maximal spin contrast will be presented and finally an outlook names the effects limiting the pEDMR spin contrast.

5.3. Pulsed Electrical Detected Magnetic Resonance on NV⁻ Centers

5.3.1. Electron Spin Resonance

Basically, the same pulse sequence as for ODMR can be used for pEDMR. Microwave pulses initialize the spin ensemble into any macroscopic superposition of $|1\rangle$ and $|2\rangle$. The read-out is conducted as follows: 520 nm laser induces transitions $|1\rangle \rightarrow |3\rangle$ and $|2\rangle \rightarrow |4\rangle$, dependent on the spin initialization. The main difference for $|3\rangle$ and $|4\rangle$ is the branching ratio r into the dark state, which reduces the signal amplitude when being occupied. Figure 5.6 shows experimental data for the expected signal reduction due to microwave induced spin transitions. pEDMR data is shown next to ODMR data, both data traces are normalized and vertically slightly shifted. The inset visualizes the dominant detection mechanism for resonant and off-resonant case, respectively. The data shown was recorded in two separate measurements differing only in the frequency sweep direction to optimize the measurement time¹. For both sweep directions a Lorentzian fit was computed. The resulting pEDMR resonance frequencies f_{pEDMR} differed by more than 10 standard deviations of the individual measurement, which is the consequence of the dime delay in the setup that is translated into a frequency shift. Since this effect is the same except the sign building the averaged mean cancels the errors and yields $f_{\text{pEDMR}} = (2.87014 \pm 0.00007)$ GHz. This value is in agreement with the optical measurement that yields for the resonance frequency $f_{\text{ODMR}} = (2.87004 \pm 0.00004)$ GHz. The contrast is comparable for both read-outs with a value of $-(12.6 \pm 0.2)\%$ for pEDMR and $-(14.4 \pm 0.2)\%$ for ODMR. The ODMR resonance linewidth is by 12 % broader than the pEDMR linewidth with $\text{FWHM}_{\text{pEDMR}} = (13.3 \pm 0.2)$ MHz. Basically the linewidth should be the same for both detection principles, as has been already demonstrated by Bourgeois et al. (2015). Narrowing of the linewidth under higher optical power has been reported, an effect explained by a change of the longitudinal versus transverse spin relaxation time. A larger FWHM for ODMR indicates then an additional signal contribution from a larger detection volume with a corresponding weaker optical power for ODMR compared to that of the pEDMR detection region.

For a simple model estimating the ODMR contrast we consider NV⁻ center ionization to happen at a longer timescale than recombination. We get

¹A signal rise / fall constant occurred in the current measurement. To record data at a high sweep rate two sweeps were recorded and analyzed separately. This results in a better effective measurement to experiment time compared to a measurement that is in perfect equilibrium for every data point.

5. Basic Experiments

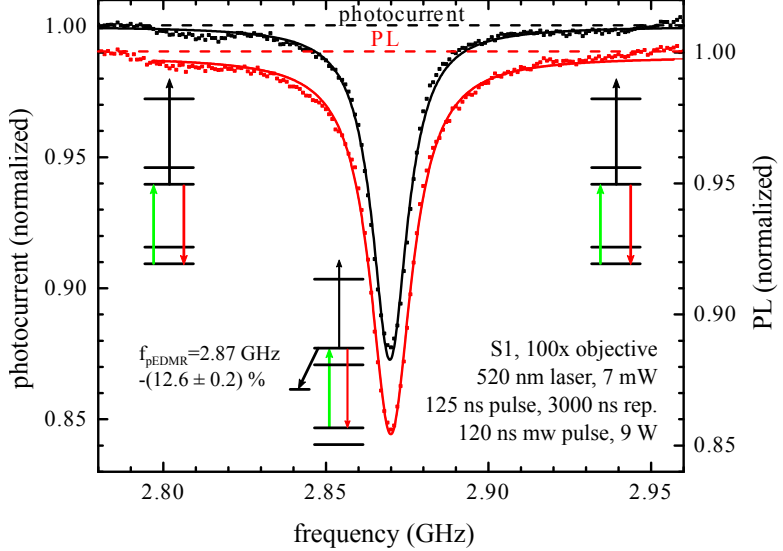


Figure 5.6.: Spin resonance is observed when the microwave excitation frequency matches the zero field splitting parameter D . After photoexcitation $|4\rangle$ has a high probability to relax into the dark state, which reduces the photocurrent. For comparison simultaneously detected ODMR is shown, the solid lines are Lorentz fits.

different branching ratios from the partial life times

$$r_{35} = \frac{\tau_3}{\tau_{35} + \tau_{31}} = 14 \% \text{, and } r_{31} = 1 - r_{35} = 86 \%$$

$$r_{45} = \frac{\tau_4}{\tau_{45} + \tau_{41}} = 50 \% \text{, and } r_{42} = 1 - r_{45} = 50 \%$$

for $|3\rangle$ and $|4\rangle$ respectively. Calculating the contrast just from the difference of these partial PL life times τ_{31} and τ_{42} yields an ODMR contrast of $\frac{86 \% - 50 \%}{86 \%} = 42 \%$. We note that this is only valid for perfect initial spin polarization and short laser pulses compared to the non-radiative dark state relaxation time. For stronger pulses the situation changes due to additional ionization and recharging effects. These are exactly the processes that have to be analyzed in the case of pEDMR. Here, the excited NV⁻ triplet state, $|3\rangle$ or $|4\rangle$, requires a second photo absorption process for the electrical read-out. The ODMR contrast can be calculated just from the population of states $|3\rangle$ and $|4\rangle$, while for pEDMR an additional photo excitation of these states is required. Since this photocurrent generation mechanism is quadratic in

5.3. Pulsed Electrical Detected Magnetic Resonance on NV⁻ Centers

laser power a characteristic difference to the optical read-out is identified. The discussion on spin contrast will be continued in section 5.3.2 including further experimental data that coincide with data and Monte-Carlo simulation published recently by Hrubesch et al. (2017). Before the discussion on maximal read-out spin contrast will be continued optimal spin initialization has to be ensured. The NV⁻ center has in its ground state a spin $S=1$ and consists of state $|1\rangle$ with $m_s=0$ and $|2\rangle$, with spin projection $m_s = \pm 1$, being degenerate at zero external magnetic field. The triplet sub-states $|1\rangle$ and $|2\rangle$ are split by $D = 0.012$ meV. At room temperature the Boltzmann distribution yields only negligible differences for $|1\rangle$ and $|1\rangle$ occupation since $D \ll k_B T = 25$ meV. Significant polarization is achieved as follows: Under green illumination shelving over the the dark state accumulates electrons in $|1\rangle$. Then a microwave π -pulse induces the transition $|1\rangle \rightarrow |2\rangle$ and shifts the major population into $|2\rangle$. Conditions for the rectangular π -pulse are the right frequency $f = D/h$ and duration t_π .

$$\nu_{\text{Rabi}} = \frac{1}{4\pi} \frac{g\mu_B B_{\text{MW}}}{\hbar} \quad (5.1)$$

the parameter t_π can be calculated as introduced in section 2.2 as the half of a full Rabi-cycle,

$$\tau_\pi = \frac{1}{2} \frac{1}{\nu_{\text{Rabi}}}. \quad (5.2)$$

Assuming a magnetic field of 1.5 mT at the NV⁻ center location one obtains $\nu_{\text{Rabi}} = 4$ MHz and thus $\tau_\pi = 125$ ns using equation 5.2. At this pulse length spin polarization is maximal and thus maximal pEDMR contrast is expected. The dynamics of spin transition between $|1\rangle$ and $|2\rangle$ can be investigated by variation of the microwave pulse duration. The contrast increases with pulse duration as $|2\rangle$ gets populated, which is observed as signal reduction, representative data is given in fig. 5.7 a). A contrast can be evaluated from the data by comparing the signal amplitude of resonant and off-resonant measurements that are separated by 4-5 FWHMs from resonance.

For f_{res} the photocurrent is reduced until an absolute minimum is reached at $t_{\text{MW}} = 120$ ns or 160 ns for the different excitation spots A and B, respectively. For longer t_{MW} the signal rises slightly again and settles at a value still more than 10 % below the signal of an off-resonantly excited system. With the observation of maximal contrast and thus spin polarization the corresponding microwave pulse duration can be set equal to t_π . For $t > t_\pi$ is still a t_{mw} -dependency on pEDMR contrast apparent before saturation that is attributed to the different spin transition within the spin ensemble. NV⁻ centers are randomly distributed among four possible crystal orientations.

5. Basic Experiments

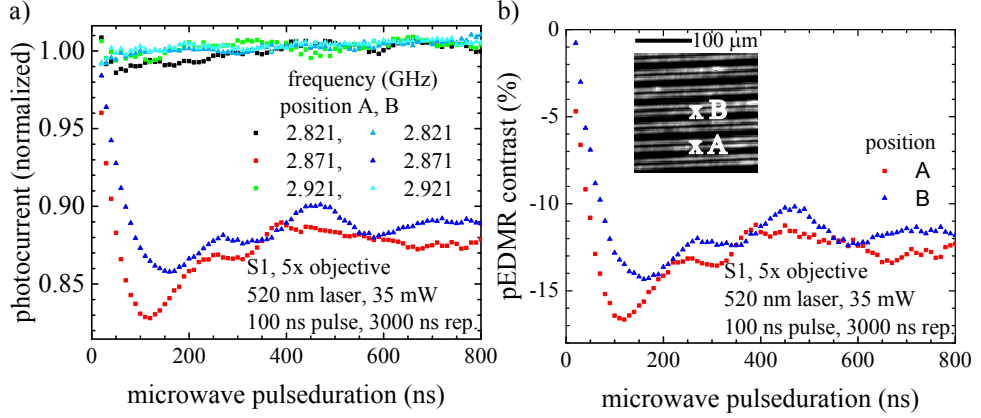


Figure 5.7.: a) Microwave induced spin transition reduce the photocurrent. Minimal pEDMR signal is observed for a microwave π -pulse , towards longer times dephasing of the spin ensemble leads to a constant offset. **b)** pEDMR contrast varies with position, where magnetic field amplitude and relative NV[−] center orientation are in-homogeneously distributed.

For one of them the projection of \mathbf{B}_{mw} on the NV[−] center axis is maximal and thus t_{π} minimal. Spin transition times for the other orientations are longer, depending on the alignment of \mathbf{B}_{mw} and the diamond lattice. From the data presented here a computed Fourier transformation could not provide significant results to study this effect in more detail. To conclude we end up with a maximal ensemble spin polarization after a microwave π -pulse of 120 ns at positions close to the first interdigital contact.

5.3.2. Optimization of pEDMR Dynamics

Once maximal spin polarization is ensured, mainly for one of four NV[−] center orientations in absence of external magnetic field, investigations of the spin to charge conversion of our method can be conducted. In order to optimize the ionization of NV[−] center with respect to the spin configuration different ionization laser powers and pulse duration are tested experimentally. For each data point in fig. 5.8 the photocurrent signals of resonant measurements at $f_{\text{res}} = 2.871$ GHz and off-resonant measurements at $f_{1,2} = 2.82, 2.92$ GHz were used for evaluation of the pEDMR contrast. The nominal optical power on the horizontal axis has been determined in a separate measurement. As explained in chapter ?? the laser power varies non-linearly with both repetition time and pulse duration. Here, the repetition time is higher than

5.3. Pulsed Electrical Detected Magnetic Resonance on NV⁻ Centers

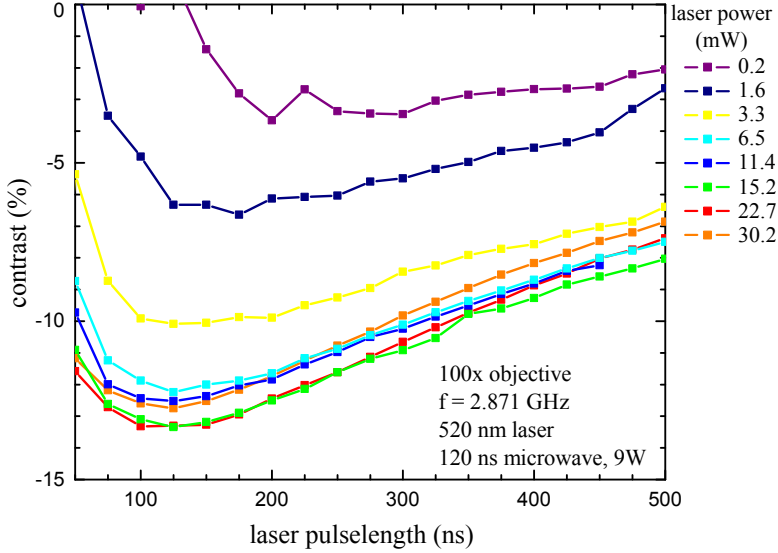


Figure 5.8.: The contrast of the NV⁻ pEDMR spin read-out strongly depends on the photoionization pulse. Optimal conditions can be identified and data interpreted with the five state model for the NV⁻ center.

in the calibration, leading to a small systematic deviation of a few percent for all laser intensities. The effect of pulselength has a much bigger impact since towards smaller pulse times $t_{\text{ion}} < 50$ ns the pulse shape deviates from a rectangle. Further, for high pulse times at high intensities heat reduced the power output of the laser. To summarize, these mentioned effects limit the determination of an accurate power and have to be interpreted as values with both statistical and non negligible systematical error.

Experimental errors introduced by laser intensity fluctuations were averaged out by subtracting a linear background signal. The mathematical expression used for pEDMR contrast evaluation is

$$\left(\frac{\Delta I}{I} \right)_{\text{pEDMR}} = \frac{I_{f_{\text{res}}} - \bar{I}}{\bar{I}}, \text{ where } \bar{I} = \frac{I_{f_1} + I_{f_2}}{2}. \quad (5.3)$$

Since spin conserving optical transitions connect states $|1\rangle \leftrightarrow |3\rangle$ and $|2\rangle \leftrightarrow |4\rangle$ in the following discussion spin polarization refers to an generalized expression including both, polarization of the optical ground plus that of optically excited state. For weak ionization pulses at laser power below 1 mW the contrast is quite low, being more pronounced for $t_{\text{ion}} > 200$ ns. At shorter pulse lengths the spin contrast vanishes due the decreasing contribution of

5. Basic Experiments

NV^- versus N_s^0 photoionization. A characteristic dependence describes the contrast for intermediate P_{ion} up to 400 mV differing only in a multiplicative constant. With rising power the spin current from $|4\rangle$ ionization is decreased by a shelving process. The dark state $|5\rangle$ is populated by many $|2\rangle \rightleftharpoons |4\rangle$ transitions, where each relaxation process has a significant probability of the branching index ~ 0.5 to be shelfed into the dark state. The same argument of increased shelving effect accounts for longer laser pulse duration, as long as relaxations from the dark state into the NV^- center ground states $|1\rangle$ and $|2\rangle$ can be neglected. With a partial lifetime of 290 ns preferably $|1\rangle$ is populated by non-radiative dark state relaxation, effectively decreasing the system's spin polarization for t_{ion} comparable to τ_{51} . In the data a maximal spin contrast is observed at $t_{\text{ion}} = 100 - 150$ ns. For this and higher t_{ion} the $|5\rangle \rightleftharpoons |1\rangle$ transition limits the spin contrast. To put the performance of electrical NV^- center spin-readout of in numbers the maximal achieved contrast is -13.5 % in this experiment for $t_{\text{ion}} = 125 \pm 25$ at 520 nm laser power of $P_{\text{ion}} = 25$ mW.

The spin selectivity of the ionization process reduces when the ionization rate approaches τ_{45} . Independent of the spin electrons tend to get ionized as soon as they are excited into $|3\rangle$ or $|4\rangle$. The consequence for $P_{\text{ion}} > 25$ mW is pEDMR contrast reduction for all t_{ion} and even stronger contrast reduction for long times. This effect can be verified by comparing the data sets for $P_{\text{ion}} = 400, 500$ mV, where significant lower contrast occurs for the high P_{ion} towards long $t_{\text{ion}} > 300$ ns. Very similar pEDMR contrast results have been obtained from experiments with more homogeneous illumination using the 5x objective, but shall not be discussed additionally here. Under the assumption that the microwave pulse did not perfectly polarize the NV^- spin ensemble in its initial state the presented results are in agreement with demonstration of pEDMR contrast of -16 % Hrubesch et al. (2017). This work additionally develops in a Monte-Carlo simulation a quantitative description of the pEDMR contrast with respect to intensity and duration of a 532 nm laser. The pEDMR contrast is found to be limited by nitrogen donor concentration in diamond and predicted to reach 40 % in absence of N_s^0 . However, most recent creation methods for NV^- centers in diamond rely on irradiation processes, that do not achieve creation of a NV^- center for each nitrogen donor. Further, deterministic creation of single NV^- centers has not been realized. In a next step will be tested, if electrical spin read-out can be optimized by integration of an additional laser pulse with higher photon energy in the pEDMR pulse sequence.

6. Dual laser excitation of the NV⁻ center

Having studied and optimized the dynamics of the NV⁻ spin to charge conversion under 520 nm laser illumination, it has turned out that nitrogen donors limit the pEDMR contrast. Further contrast improvement might be achieved by separating and resolving the different excitation steps in time and photon energy. Section 6.1 shows absence of pEDMR contrast for a purely blue laser induced spin read-out. Further findings do not indicate any contrast improvement when combining green and blue laser excitation and will be explained by a comparatively high blue laser photon energy directly ionizing the NV⁻ center ground state, regardless of its spin orientation.

Another approach is to tune E_{ph} for NV⁻ photoionization to prevent the parasitic NV⁰ photocurrent contribution. A first proof of principle experiment opening the way for further investigation is demonstrated in section 6.2.

6.1. 520 nm and 450 nm Dual Laser NV⁻ Ionization

In the first section it is shown experimentally that in diamond photocurrent generation is dominated by absorption of one photon for blue 450 nm laser excitation. In a next step a pulse sequence comparable to the green laser driven pEDMR experiment is introduced and discussed. In a last step the assumption of direct NV⁻ ground state ionization is underlined by an experiment demonstrating reduction of pEDMR contrast.

6.1.1. Alignment of Laser Spots

The entire set of pEDMR experiments described in this chapter is performed using the 100x objective. The axial position of laser spots is determined

6. Dual laser excitation of the NV⁻ center

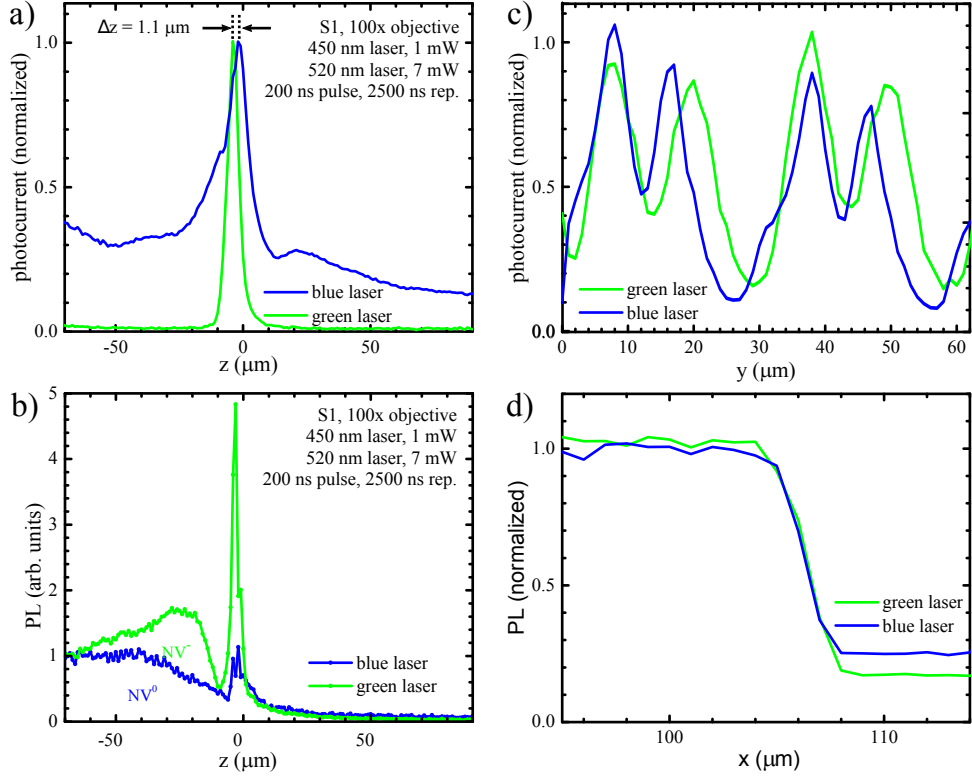


Figure 6.1.: a),b) Maximal photocurrent or PL signal is observed when the laser spot is close to the surface, allowing for identification of an axial offset. **c), d)** Overlap of laser spots can be followed from lateral scans across interdigital contacts.

utilizing sample S1 by z -scans close to the surface. Data of the corresponding photocurrent and PL signal is shown in fig. 6.1 a) and b).

From the signal generated by green laser excitation one deduces the position of the diamond surface with the method described in section 5.2. The photocurrent signal for blue laser excitation is not only shifted slightly in axial direction, but differs characteristically in its shape. A maximum is observed at z shifted by $1.1 \mu\text{m}$ with respect to the green laser, indicating that the focal length is $1.1 \mu\text{m}$ larger for the blue laser spot than for the green one. As we will see later on, there is no quadratic power dependence for the blue laser, resulting in a broader current peak, even though the point spread function is comparable. It can be verified from the data that small laser intensity is capable of producing a detectable photocurrent when the laser is defocused

6.1. 520 nm and 450 nm Dual Laser NV⁻ Ionization

by 100 μm . In that case the laser illuminates an area of about 210 μm in diameter. A large weakly illuminated diamond volume close to metal contacts then generates photocurrent under blue laser illumination whereas a higher green laser power density does not produce detectable photocurrent. The PL signal exhibits pronounced maximums at the same positions as the photocurrent signal does. The shape differs characteristically, since under 450 nm illumination no longer NV⁻ but NV⁰ is the preferred charge state and the optical excitation mechanisms are different. Having defined the surface plane the relative lateral position of both laser spots can be minimized by shifting the blue laser spot in x - and y -direction. Micrometer drives on kinetic mirror mounts allow for precise manual alignment. Fig. 6.1 c exemplary depicts the laser induced photocurrent signals after laser alignment in y -direction. Since the axial scan has shown the difference in focal length for the lasers, an objective working distance is chosen where both lasers illuminate a comparably large volume. The slightly defocused laser spots generate a broadened photocurrent signal with characteristic maximums and minimums that can be matched. A difference in peak to peak distance and peak levels can be explained by two effects. Firstly, different peak heights indicate a deviation of laser propagation direction and diamond surface, an effect that occurs for both lasers. Secondly the peak spacing is about one third larger for the green laser, indicating different spot sizes or photocurrent generation mechanisms. After positioning, the remaining lateral displacement in y -direction is about $(2.0 \pm 0.5) \mu\text{m}$, when the left side of the contacts is chosen as measurement position, and $(0.2 \pm 0.2) \mu\text{m}$ in x -direction, as deduced from PL data (fig 6.1 d). Considering the laser spot displacement $<2 \mu\text{m}$ in three dimensions and beam diameters of about 2-3 μm under the given experimental conditions a partial overlap of both lasers is not guaranteed. For the following experiments we chose a working distance where both laser spots penetrate the sample by at least 1 μm creating a situation with increased partial overlap of illuminated detection volume. Basically the method described here allows for precise determination of laser spot sizes, positions and directions by interpreting three dimensional photocurrent scans with a resolution close to the diffraction limit.

6.1.2. 450 nm Laser Photoionization of the NV⁻ Center

In section 5.2.1 the two photon ionization of the NV⁻ center has been discussed for a 520 nm laser. Here, we investigate the NV⁻ center photoionization under 450 nm laser excitation with the same experimental conditions as used for the 520 nm excitation in section 5.2.1. The blue photon energy

6. Dual laser excitation of the NV^- center

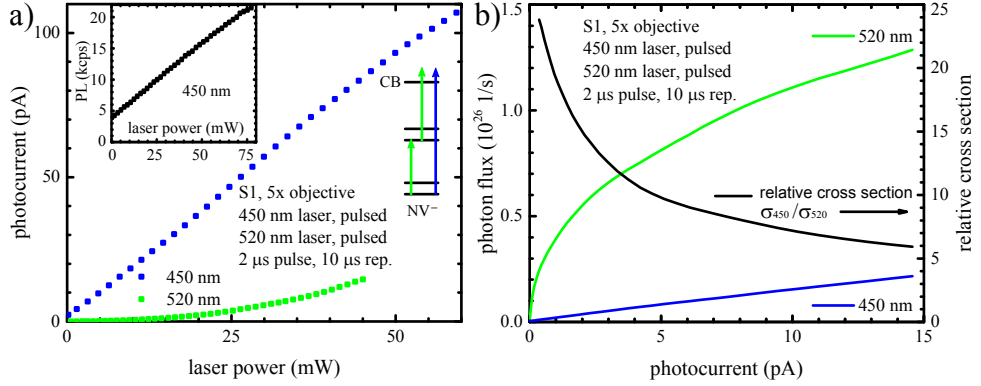


Figure 6.2.: a) Blue photons promote directly electrons from NV^- to the conduction band. The observed linear power-dependency suggests a process dominated by one photon excitation, as visualized in the inset. For comparison the previously discussed two photon ionization by a 520 nm laser is shown. **b)** The cross section inversely proportional to photon flux is larger for 450 nm irradiation and varies with the photocurrent level. The small photocurrent offset arising from the amplifier, is corrected in b).

$E_{\text{ph}} = 2.76 \text{ eV}$ is now higher than $E_{\text{ph}} = 2.38 \text{ eV}$ of green photons. The experimental finding of a linear photocurrent and PL dependence on laser power is shown in fig. 6.2 a. The origin of the non negligible offset in the PL data can not be assigned to a background signal and is not yet fully understood.

From the detection of photocurrent itself it is followed that both ionization of NV^- and recharging, $\text{NV}^0 \rightarrow \text{NV}^-$, is driven by 450 nm photo-absorption. The photon energy is with 2.75 eV only slightly larger than half of the diamond band gap energy. For the characterization of the photocurrent versus laser power homogeneous illumination of diamond is realized with the 5x objective. In order to suppress pulse artifacts a pulse length much longer than internal transition rates is used. A value of $t_{\text{ion}} = 2 \mu\text{s}$ is chosen at a pulse sequence repetition time of $10 \mu\text{s}$. A linear power dependence for 450 nm photoionization suggests that one optical transition is rate limiting. Due to a high density of states in the valence band electron excitation is faster than ionization from a defect state within the band gap. This is the same argument as used for the previously discussed nm photoionization in section 5.2.1. Thus the rate limiting transition is identified to be $|1\rangle$, $|2\rangle$ into the conduction band for 450 nm photons. However, we cannot experimentally exclude a photocurrent contribution from nitrogen donor ionization. The ar-

6.1. 520 nm and 450 nm Dual Laser NV⁻ Ionization

gument allowing for neglect of N_s⁰ photocurrent cannot be the ionization rate but a small N_s⁺ → N_s⁰ recombination rate of conduction band electrons. A two photon absorption process for valence band electrons over virtual states in the band gap can also be neglected. This argumentation can be concluded with the experimental finding of a N_s⁺ → N_s⁰ recombination rate in the range of Hertz, several orders of magnitude smaller than N_s⁰ ionization rate Chen et al. (2017). Another finding is that the detected photocurrent is larger by more than one order of magnitude for $P_{\text{ion}} < 40$ mW, but with quadratically increasing photocurrent for the green laser this ratio decreases. The photoabsorption cross section has been investigated for type IIa diamond as a function of E_{ph} by Rohrer (1998). A constant photocurrent method was utilized, where the photocurrent is stabilized at a constant level as E_{ph} varies. The photon density is measured and shown to be not an absolute but relative dependence of cross section versus E_{ph} . The cross section is reported to rise significantly by a factor of (4 ± 1) when increasing E_{ph} from 2.34 eV to 2.76 eV. This is in agreement with the our findings (fig. 5.3 b) assuming a quadratic power dependency for 520 nm laser induced photocurrent when P_{ion} is set to (60 ± 10) mW at a photocurrent level of 0.4 nA.

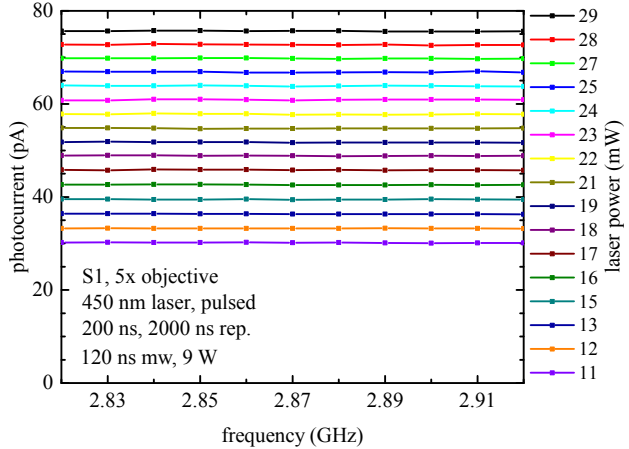
6.1.3. Pulse Sequence for Green and Blue Laser Assisted pEDMR on NV⁻ centers

A similar experiment according to the previously discussed pEDMR under 520 nm laser excitation is set up with the 450 nm laser. The pulse sequence used is basically the same as in section 5.3.2 and is depicted schematically next to the data in fig. 6.1.3. Photoionization pulse parameters P_{ion} and t_{ion} are close to those settings for maximal pEDMR contrast of about -13 % under green illumination.

For a range of blue laser powers $P_{\text{ion}} = 11 - 29$ mW both pEDMR and ODMR is recorded. For none of the data sets a significant spin contrast <-1 % is detectable. We note that a 450 nm laser induced PL signal is detected, as already mentioned in 6.1.2. Observation of no ODMR contrast can be interpreted as follows: If electrons are excited to states |3⟩ and |4⟩, they would undergo spin dependent inter system crossing into |5⟩, from where they relax dominantly non-radiatively. This transition reduces the observed PL intensity. Since no spin contrast is observed, one concludes that the observed PL signal does not exclusively originate from the NV⁻ PL spectrum. In fact it is known that NV⁰ ⇌ NV⁻ charge state conversion depends on the excitation wavelength Aslam et al. (2013), Beha et al. (2012). For photoexcitation at 450 nm the dominant charge state is NV⁰ Aslam et al. (2013). At this

6. Dual laser excitation of the NV⁻ center

Figure 6.3:
No pEDMR contrast can be detected when blue laser induces NV⁻ ground state photoionization and recharging, NV⁰ → NV⁻.



excitation wavelength NV⁰ can be excited and outperform possible NV⁻ PL. However, sophisticated discussion on the PL signal can only be continued with further, spectrally resolved, PL data. When the 450 nm laser induced photocurrent is considered, similar arguments as for the PL discussion can be used. The main part of photocurrent can be attributed to NV⁻ → NV⁰ conversion and the absence of spin selectivity can be attributed to photoionization from the NV⁻ ground state, independent of the spin.

In a next step a pulse sequence is introduced where both processes, NV⁰ → NV⁻ conversion and NV⁻ → NV⁰ ionization are combined by integrating two lasers in the experiment. The read-out pulse sequence is designed to consist of a 520 nm laser shelving pulse followed by a 450 nm ionization laser pulse and is concluded by a set of NV⁰ recharging pulses, as depicted in fig. 6.4 b. Using results from the pEDMR optimization (see section ??) as an estimate for starting conditions, values of 50 ns for laser pulse duration and 12 ns for the delay are chosen at intermediate laser powers. To adapt the laser intensities the total photocurrent integrated over many pulse sequence repetitions is investigated from the data in fig. 6.4 a. At zero blue laser power the quadratic phococurrent dependency on green laser power can be identified on the left vertical axis, as discussed in section 5.2.1. Accordingly the approximately linear power dependence for the blue laser is represented by the lowest data set along the horizontal axis. Deviations from linearity stems from inaccurate determination of the laser power, that depends strongly on intensity, duration and repetition rate and has not been calibrated separately, but extrapolated from a related calibration measurement. At the first sight the photocurrent signal seems to be a superposition of the photocurrent induced by single lasers. That would exclude any interaction

6.1. 520 nm and 450 nm Dual Laser NV⁻ Ionization

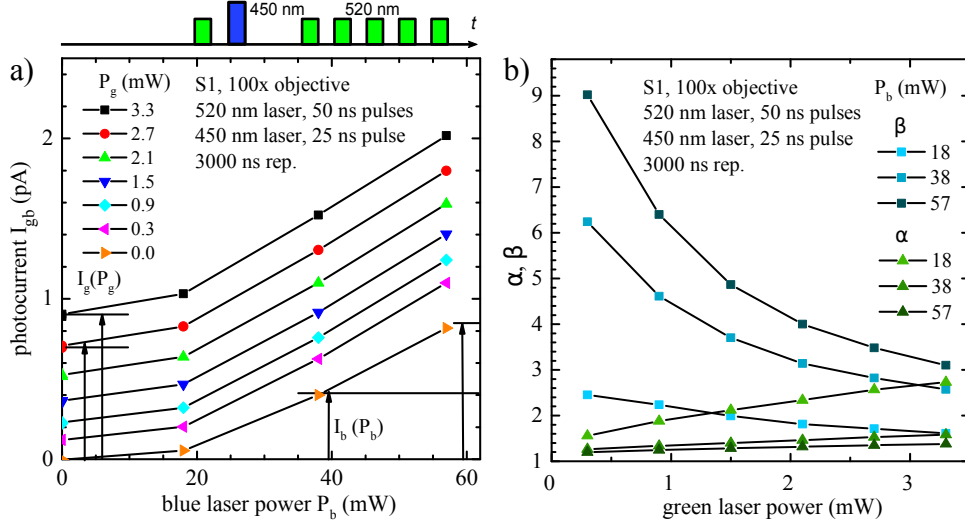


Figure 6.4.: a) A pulsed sequence designed for pEDMR experiments is tested for different laser powers. **b)** Interactions of both lasers at the NV⁻ center occur as non-linearity of the coefficients introduced here.

of green and blue laser light within a pulse sequence. A simple model with two characteristic parameters is introduced allowing for more detailed investigation of the interaction. The total observed signal I_{gb} is compared to the photocurrent contribution I_g , I_b attributed to the green and blue laser, respectively. Parameters α and β are defined as¹

$$\alpha = \frac{I_{gb} - I_g}{I_b} \text{ and } \beta = \frac{I_{gb} - I_b - 5/6 \cdot I_g}{I_g/6}, \quad (6.1)$$

and describe a normalization on the photocurrent induced by the very first pulse for each laser in the pulse sequence. Without any interaction, thus $I_{gb} = I_g + I_b$, both parameters equal one. Any deviation from one has to be attributed to nonlinear effects and increases the parameter. Figure 6.4 b shows α and β as a function of P_b for different P_g . A parameter of our simple model with dependence on both laser powers indicates occurrence of nonlinearities. Before discussing physics the errors of this evaluation have to be considered. Normalization on small currents gives rise to big multiplicative errors. Further the attributed laser powers are defective and the effective overlap remains unknown, allowing only for limited quantitative analysis.

¹The fractions 5/6 and 1/6 are adapted to the pulse sequence consisting of 6 pulses that are assumed to contribute equally and independently to I_g .

6. Dual laser excitation of the NV⁻ center

For α a value slightly larger one can be identified, increasing weaker than linearly with P_g . The increase is more pronounced for less P_b . An explanation for this dependence is blue laser induced photoionization of |1> and |2>, that becomes more efficient with P_g . The ionization with respect to the blue laser induced photocurrent becomes maximal under conditions of comparatively low blue laser power <18 mW and high green laser power $P_g > 0.15$ mW. Here, P_b is still low enough not to dominate the NV⁰ → NV⁻ recharging process, which is more efficient for 520 nm excitation.

The parameter β neglects the amplitude of the blue laser induced photocurrent and thus increases with both increasing P_b and decreasing P_g . In this context amplification of the photocurrent induced by the first green laser pulse is maximized as the blue ionization energy is large and the green laser power goes to zero. The observed trends for for maximization of α and β are competing. The contrary trends are just a consequence of the parameter definition and are not appropriate for accurate description of the data. However, a model with an additional interaction term linear in P_g and P_b was considered as well for the interpretation but did not agree with the observed parameter values for α and β . A more complex experiment is conducted to identify the nature of the NV⁻ ionization processes in terms of spin sensitivity. To the previously presented pulse sequence just a microwave pulse is added to initialize the NV⁻ center spins. Simultaneously recorded pEDMR and ODMR can be analyzed and allow to identify three different physical regimes for the spin contrast. Figure 6.5 a depicts pEDMR data for small P_g . For even lower P_g no pEDMR contrast is detectable. According to the concepts presented in section 5.3 the contrast increases with P_g , but is lowered by the additional influence of the last fife recharge pulses in this extended pulse sequence.

A significant contrast reduction occurs for large blue ionization powers above 20 mW. At this threshold 450 nm photoionization begins to outperform photoionization driven by the 520 nm laser. The most probable charge state becomes NV⁰ and any NV⁻ population is immediately converted into NV⁰ again. In the limit of very high P_b where P_g is negligible any green laser the contrast will disappear, as already discussed in the case of purely blue laser induced pEDMR. The effects observed in the pEDMR data can be identified to begin at the same threshold as for ODMR and at which 450 nm photoionization sets in (fig. 6.4 a). There is no intermediate regime where the 450 nm ionization by blue laser does outperform 520 nm ionization without abrogating the shelving process.

6.2. Green Red Excitation

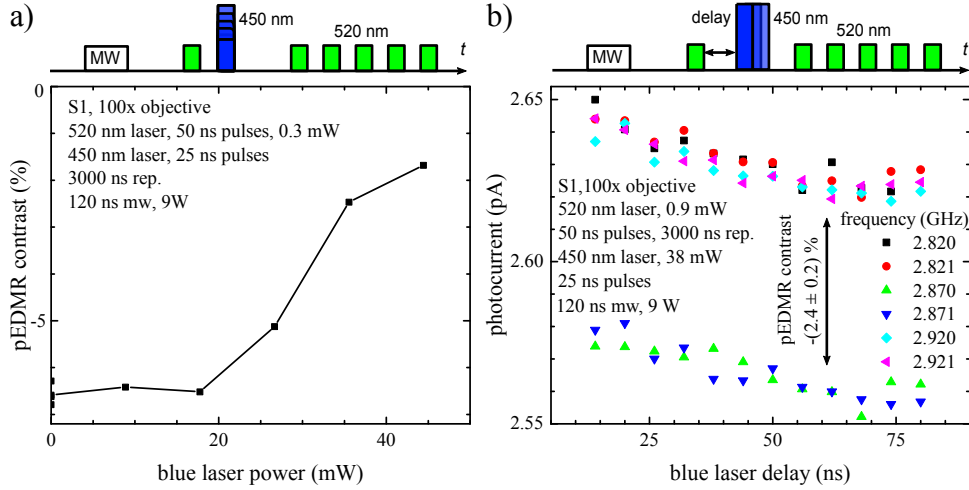


Figure 6.5.: a) Combined laser illumination shows quenching of pEDMR contrast under strong blue laser excitation. There, regardless of the spin state NV^- ground state electrons are excited to the conduction band. **b)** Variation of the 450 nm laser pulse delay shows no characteristic dependence on the laser power, supporting the model of an independent ionization process of the NV^- center.

6.2. Green Red Excitation

In section 5.3.2 the effect limiting pEDMR contrast to a value close to -20 % is assigned to be N_s^0 ionization. Here, absence of a N_s^0 photocurrent is presented for a near infra red (NIR) laser with E_{ph} slightly smaller than the nitrogen defect ionization energy. Our finding is in agreement with other independently reported results and allows to circumvent the limiting effect not by changes of the diamond substrates or NV^- center creation process but by adaption of the pEDMR read-out method Chen et al. (2017).

6.2.1. Laser Alignment

For a homogeneous illumination the 5x objective is chosen. Excitation laser wavelengths are 520 nm for the green laser and 785 nm for the NIR laser. Pure green illumination generates a photocurrent, whereas the near infra red laser does not. Therefore alignment was optimized using a material with lower band gap, SiC, where 785 nm photons generate a photocurrent by ionization of the single silicon vacancy in a process comparable to NV^- center

6. Dual laser excitation of the NV⁻ center

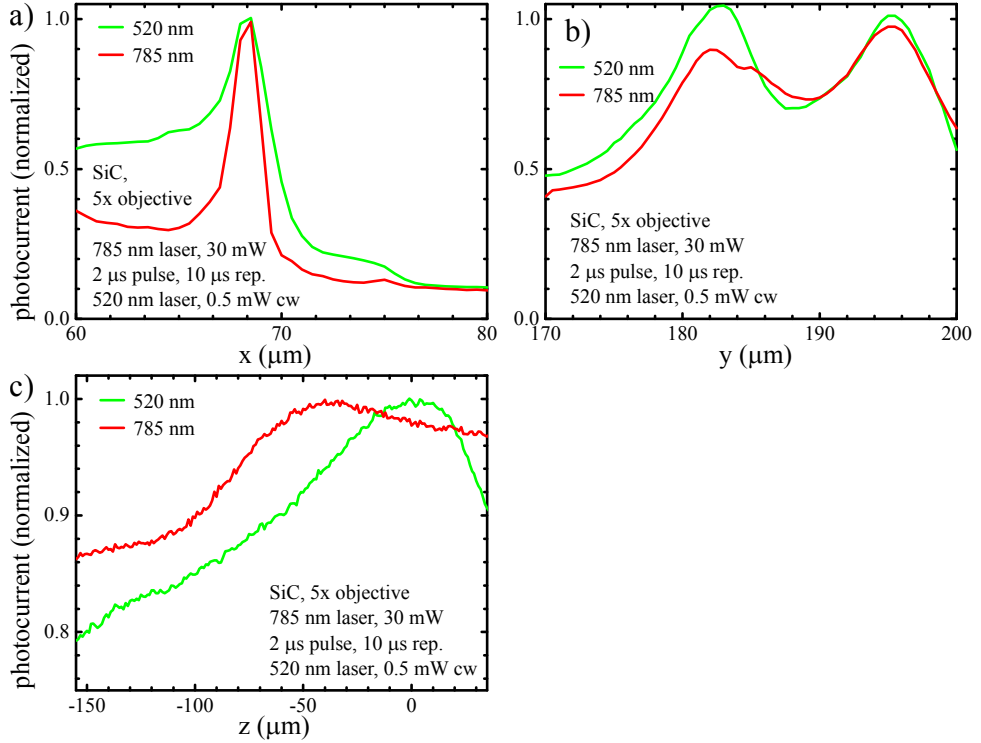


Figure 6.6.: Alignment of NIR and green laser. a), b) Scanning across interdigital contacts allows to determine the relative laser position offset. c) The axial spot positions deviate by $(35 \pm 5) \mu\text{m}$.

ionization in diamond Fuchs et al. (2017). In diamond the 5.45 eV of band gap energy is overcome by in total four photons of 2.34 eV, while in SiC 3.23 eV can be overcome by three 1.58 eV photons. The first photon excites, a second ionizes and a third recharges the defect into the initial state. Information on the energy levels of the 4H-SiC divacancy were taken from Hain et al. (2014). Another photocurrent contribution comes from ionization of substitutional nitrogen. Nitrogen in 4H-SiC is a shallow donor with ionization energy of 45 meV which is low compared to previously discussed defect levels in SiC or diamond Götz et al. (1993). Conditions for operation of the silicon carbide MSM detector are adopted from the diamond device. The same procedure as for the laser spot alignment on diamond can be applied on Silicon. This time the 5x objective illuminates a larger area, allowing for a better overlap of volumes illuminated by the green and red laser. When the SiC sample surface is in focus, a lateral x -scan parallel to

6.2. Green Red Excitation

the interdigital contacts is performed. Data after red laser alignment in x -direction is shown in fig. 6.6 a. The feature at $68 \mu\text{m}$ marks the inner edge of the positively biased supply contact. To higher z there is small photocurrent detected up to $75 \mu\text{m}$ and a drop to an absolute minimum for even higher values. The metal contact prohibits photocurrent generation by covering the detector material underneath. From the still increased photocurrent in the range $z = 69 - 75 \mu\text{m}$ laser spot blurring of up to $6 \mu\text{m}$ can be followed. This value is acceptably close to $9 \mu\text{m}$, the expected spot size for the 5x objective and a 785 nm laser. In y direction the alignment procedure is repeated, resulting in a good match when scanning between two negative and one positive interdigital contacts at positions 175, 205 and 190 μm , respectively (fig. 6.6 b). Maximal signal is expected close to the positive contact, the width is increased as a consequence of the spot size.

In the focal plane the laser spot centers deviate by less than $0.5 \mu\text{m}$, which is much smaller than the spot size. In axial direction a correction of focal depth is not possible in our setup. However the deviation can be measured (fig. 6.6 c), revealing that the green laser has a $50 \mu\text{m}$ higher focus length than the red laser. From $\text{NA} = 0.15$ a laser spots widening of $4 \mu\text{m}/25 \mu\text{m}$ can be calculated. For further experiments an intermediate z -position of $-17 \mu\text{m}$ was chosen. Estimated spot diameters for this setting are $17 \mu\text{m}$ for the NIR and $14 \mu\text{m}$ for the green laser.

6.2.2. Dual Laser Photoionization Protocol prohibiting N_s^0 Ionization

In a pulsed experiment the photoionization in diamond by a NIR laser is investigated. The photon energy is smaller than the threshold energy for N_s^0 ionization of 2 eV . One tries to ionize the optically excited NV^- center that is energetically about 0.6 eV below the conduction band, as one can deduce from E_{ph} of ionizing 450 nm photons and the ZPL emission at 637 nm. Further, the optically excited NV^- center is reported to be 2.7 eV below the band gap, being studied in a indirect method Aslam et al. (2013). Another group of scientists deduces from cross section measurements a ionization energy of $2.66\text{-}2.70 \text{ eV}$ Bourgeois et al. (2017). The NV^- center model would allow green photons to recharge and excite the NV^- center. A powerful NIR laser pulse could then be applied to promote the electron to the conduction band. There is no certain probability of ionizing N_s^0 because it is energetically forbidden, contrary to 520 nm ionization. However, the data in fig. 6.7 provides no evidence for such a process. Independent of the red power all detected photocurrent is just induced by the green laser. In a simple picture

6. Dual laser excitation of the NV^- center

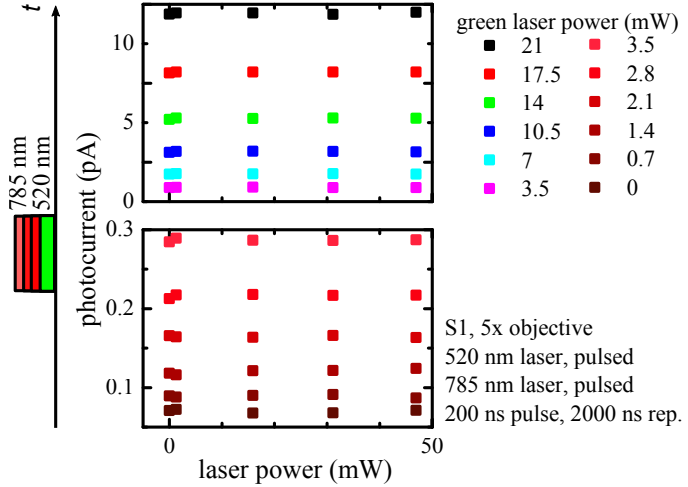


Figure 6.7.: No significant change of photocurrent was observed when a NIR laser and green laser together were focused on the sample. The reason for the independence observed here is insufficient alignment accuracy. However, one finding is that the NIR laser does not induce photoionization, explicitly it does not ionize N_s^0 .

the ionization rate, dependent on the photon flux as long as the transition energy is available should be doubled, when NIR and green laser operate at the same photon flux. At least can be seen verified here, that NIR laser does not ionize any defects at all, especially not N_s^0 . The independence of both lasers could later be referred to a mismatch of laser spots that shifted in an uncontrolled manner over days. Accordingly, in a pEDMR experiment also no effect on the pEDMR contrast could be measured. Figure 6.8 shows a weak spin contrast of -3%.

This contrast remains, even under NIR laser illumination, but the noise in the system increases drastically with NIR laser power p_{NIR} . The noise source can not be identified to be heat transported by the red laser because Schott noise in semiconductors is proportional to temperature. The noise level varies by a factor of ten that can not be attributed to the temperature T in the sample. An effect more sensitive to T is thermionic emission of electrons into the contacts. The current through a metal-semiconductor contact is characterized by the Richardson constant and a quadratic T dependence (Sze and Kwok (2007)). The quadratic T dependence allows temperature fluctuations to be still considered to influence the photocurrent amplitude, ultimately induced by unstable NIR laser mounting.

6.2. Green Red Excitation

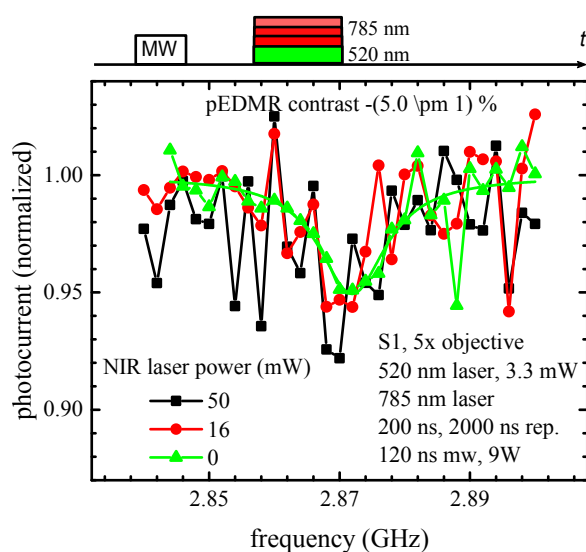


Figure 6.8:
pEDMR contrast remains under simultaneous green and NIR laser illumination. Additional noise is introduced by the NIR laser, acting as an uncontrolled heat source.

7. Outlook and Conclusions

At the beginning of my master thesis' research phase I built up a spectrometer for NV⁻ spin detection. Either optically or electrically a spin contrast can be detected by pEDMR or ODMR. Here I sum up possible extensions and improvements for the setup created. The optical detection allows to measure NV⁰ and NV⁻ PL, albeit without the possibility to distinguish just by the count rate. Additional usage of appropriate PL filters would allow for distinction between different PL emitting defects. Filters could be mounted on a rotatably wheel in the optical path before the APD. Another alternative would be recording the time dependence on the PL signal. So far time dependence is only discussed as a result of the pulse sequence design. Discussion on the PL signal can be extended, when the time information of detected photons is taken into account. The currently used data acquisition card allows for read-out at 80 MHz. The benefit would be a time resolved PL signal that reveals life times of the PL emitters. This opens an alternative approach to identify the PL emitter without the need of recording a spectrum, given that the half times are known. The time resolution can be obtained from the APD performance and the read-out device. Currently, the relevant hardware specifications are 10 ns APD pulse width, a detector dead time of 22 ns and a 80 MHz read-out card. Theoretically these parameters result in a 12 ns time resolution when integrating PL over many pulse sequences.

So far laser reflections from the sample surface are partially recognized by the APD. Better filters are required to suppress efficiently the excitation source and to transmit only PL photons. Further for the aligning of laser spots with respect to the sample structure and eventually a second laser optical feedback were helpful, as it accelerates the laser alignment process. By mapping the sample surface on a ccd-camera chip one could obtain easily optical feedback. The concept is to insert an additional beam splitter in the optical path to couple the lasers, for example using an 90/10 beam splitter. A optical density filter protects the camera chip that detects the image of the sample surface. To obtain a resolution better than the minimal laser spot size an appropriate microscope objective and ccd-chip pixel size have to be

7. Outlook and Conclusions

chosen. Another advantage of a camera imaging system is simplified sample positioning. Once there is a beam splitter in the optical excitation path, it can be used to couple in a light source and to use surface reflections to bring the sample into focus at the desired structure, benefiting from fast optical feedback in video quality. One could imaging a aligning procedure, where firstly one uses the light source to position the sample on the optical table. When the sample image is sharp, it is in the objective's focus. When two lasers are to be aligned an OD can be inserted in the camera path. Using a pulse sequence where alternating lasers illuminate the sample at a slow rate that is not to fast for the human eye the laser positions can be readjusted. Laser pulse shape and amplitude are not well defined for short pulses with $t_{ion} < 50$ ns. The power calibration conducted so far is not recommended for further experimental studies aiming for a precise description on laser power due to the high errors that arise only by small changes in the pulse sequence. For example, implementing an additional green laser recharge pulse results in a chance of the repetition rate or varies the waiting time before repeating the pulse sequence. Anyway, the duty cycle varies and causes deviation from previously conducted calibration. A photodetector in the optical path detecting laser light can track the laser intensity during the measurement and provide information on the actual absolute laser power, when losses in the optics are corrected. Light can be coupled out by using a beam splitter and a powermeter, for example integrated in the optical path before the ccd-camera.

Another, rather minor, disadvantage of the laser driver module is a minimal threshold current that is provided at any time and causes spontaneous laser diode emission. To circumvent this side-effect currently a small resistor is soldered in parallel to the diode. Below lasing threshold the laser module driver current bypasses the diode through the resistance, while it has no further effect, when the diode is lasing. Another solution without the need of hardware modification is setting a negative pulse low voltage to a value, that prevents lasing and does not harm the laser driver circuitry.

When focused laser excitation is discussed both laser spot size and power are important. The shape of the laser spot after the microscope is defined by the incident laser beam profile. Similar spot shapes are especially important, when two laser spots are to be overlapped. Smallest spot sizes are obtained for Gaussian beam profiles, that can be gathered from imperfect light sources by filtering out all non Gaussian contributions. Such a filtering mechanism is provided by a spatial filter consisting of two coplanar lenses and a pinhole in its foci. The optimization of the spot profile is achieved at the cost of laser intensity, which is reduced by the laser beam components

filtered out. Another beam profile adaption ansatz which basically conserves laser intensity is to utilize two prisms to reduce the elliptic aspect ratio. In spin resonance experiments was demonstrated that electrical read-out of the NV⁻ center in diamond provides a spin contrast that competes with optical read-out. The linewidth of spin resonance experiments is slightly different in our experiments, an effect that is not of physical origin and can be attributed to differences in detection volume and excitation intensity, as they occur only specifically in our experiment. The amplitude of spin contrast can be maximized to -13.5 % in a type IIa diamond sample. This relates to conditions where the 520 nm laser effectively pumps electrons into the dark state where they are protected from ionization for a time longer than the laser excitation pulse. From photocurrent spectroscopy experiments (sec. 6.1.2) can be deduced the one photon ionization of the NV⁻ center in its ground state by a 450 nm laser. Extended experiments with a NV⁻ read-out scheme utilizing a 520 nm and 450 nm lasers could not improve the spin contrast. As ionization power of the blue laser becomes significant, spin contrast is reduced, in accordance with an ionization mechanism completely independent on previous NV⁻ center initialization. Within the uncertainties ionization from the dark state by 450 nm laser cannot be excluded. However, this process was not reported in literature so far. So far can be concluded, that at an intermediate shelving power of less than 1 W of P_g no contrast improvements were observable. The dynamics of the entire pulse sequence may be studied in more detail to identify the preferred NV⁻ charge state during the pulse sequence. Of major importance for such experiments is the laser power and pulse shape when experimental data has to be fitted to new models. To sum up, our findings are in agreement with a strong ionization behavior of 450 nm laser resulting in a dominant NV⁰ configuration whereas 520 nm laser converts NV⁰ into NV⁻ and drives the shelving process.

Optical experiments show that utilization of a multi photon excitation mechanism improving spin contrast and high signal to noise ratio for room temperature single shot spin read-out Shields et al. (2015), Hopper et al. (2016). In analogy to optical detection techniques one could improve the electrical read-out scheme using a multi photon spin to charge conversion assisted by a red or NIR laser. Careful analysis of the laser powers allow for identification of nonlinear effects and saturation regimes. Ultimately a combination with single electron transistors fabricated on top of single NV⁻ centers this opens a route to electrical demonstration of single shot spin to charge conversion at room temperature.

7. Outlook and Conclusions

A. Laser Characteristics

A.1. Mathematical Discussion on Laser Calibration

Rectangular pulses from the signal source exhibit finite pulse flanks. The used wave form generator can reduce these triangular flanks to edge times of at least 5ns. Since most experiments deal with the value of laser power its average dependent on the experiment parameters shall be considered here in detail. A exemplary pulse is depicted in figure A.1 The averaged laser power P is defined as

$$\bar{P} = \frac{\int_0^T P(t)dt}{\int_0^T dt} \quad (\text{A.1})$$

where T denotes the integration time, in our case set to the laser repetition rate. In a simplistic case the laser driver voltage is proportional to the laser input voltage. Figure A.1 a) shows a rectangular pulse of width w and finite edge time e which can be written as

$$P(t) = \begin{cases} P_0 \cdot \frac{t}{e} & , 0 < t < e \\ P_0 & , e < t < w \\ P_0 \cdot \left(1 - \frac{t-w}{e}\right) & , w < t < w+e. \end{cases} \quad (\text{A.2})$$

Averaging $P(t)$ over time as described in eq. (A.3) yields

$$\bar{P} = \frac{1}{T} \left[2 \int_0^e P(t)dt + \int_e^w P(t)dt \right] = P_0 \frac{1}{T} \left[2 \frac{e^2}{2e} + (w-e) \right] = P_0 \frac{w}{T} \quad (\text{A.3})$$

This result can be easily verified by considering the area under the graph of $P(t)$.

Typically lasing occurs only above a lasing threshold current corresponding to U_{th} . Primed variables U' and P' are introduced as $U' = U - U_{\text{th}}$ and $P' = P(U') \propto U'$, depicted also in the right hand side of figure A.1 b).

A. Laser Characteristics

Since lasing does not start before U' exceeds 0 the effective interval of lasing is shortened. Mathematically the power can be parametrized as

$$\overline{P}' = \alpha \begin{cases} P_0 \cdot \frac{t}{e} & , 0 < t < t_0 \\ P_0 & , e < t < w \\ P_0 \left(1 - \frac{t-w}{e-t_0} \right) & , w < t < w + e - t_0. \end{cases} \quad (\text{A.4})$$

When evaluating \overline{P}' similarly to \overline{P} one obtains

$$\overline{P}' = \frac{1}{T} \left[2 \int_{t_0}^e P'(t) dt + \int_e^w P'(t) dt \right] \quad (\text{A.5})$$

$$= \frac{P_0}{T} \left[2 \frac{(e-t_0)^2}{2(e-t_0)^2} + (w-e) \right] \quad (\text{A.6})$$

$$= \frac{P_0}{T} \left(w - \frac{U_{\text{th}}}{U_0} e \right) \quad (\text{A.7})$$

$$= P_0 \frac{w}{T} \left(1 - \frac{U_{\text{th}}}{U_0} \frac{e}{w} \right) \quad (\text{A.8})$$

The result may be checked in the mathematical limits

$$\lim_{U_{\text{th}} \rightarrow 0} \overline{P}'(U') = \frac{P_0}{T} w \quad \text{and} \quad \lim_{U_{\text{th}} \rightarrow U_0} \overline{P}'(U') = \frac{P_0}{T} (w-e). \quad (\text{A.9})$$

As one would expect we obtain for $U_{\text{th}} \rightarrow 0$ the initial eq. (A.3) where no U_{th} was taken into account. The other limit can be understood graphically. For very high U_{th} lasing occurs only when U' is maximal for the interval of $w-e$. Concrete values of the lasing threshold are (100 - 200) mV for operation voltages between (100 - 700) mW corresponding to $0.14 \lesssim U_{\text{th}}/U_0 \lesssim 1$. These values lead to the conclusion that the averaged laser power scales as $P_0 w/T$ as long as the laser driver voltage is not too close to the lasing threshold and pulse width exceeds the edge time by far. Otherwise eq. (A.8) may be applied.

A.2. Laser Power Calibration

A.2. Laser Power Calibration

In this section laser voltage and laser driver voltage shall be used as synonyms for simplicity, even though this nomenclature is nonphysical. Laser intensity is measured either with a Si photodiode (*thorlabs*, S130C) or a thermal sensor (*thorlabs*, S401C). For analysis of the pulse shapes a fast Si diode (*hamatsu*, H9055) with a risetime <1 ns was used. All sensors detect a signal linear in the input power (figure A.2). Absolute values could not be obtained from data recorded with the fast Si diode, most probably because the laser could not be focused efficiently on the small detector chip. There is an increase in laser driver module performance observed at very high repetition rates, shown in fig. A.3. Further graphs provide the calibration curves for the individual laser diodes in different operation modes.

A.2.1. Blue Laser

A.2.2. Green Laser

A.2.3. NIR Laser

A.3. Laser Suppression in the Photon Detection System

A calibration of the APD detection system was conducted. For this purpose a mirror instead of the sample was mounted and the microscope objective was brought into focus. In this configuration a z -scan was recorded revealing the position of the mirror surface. For increasing laser power the mirror reflected light that enters the APD system is detected. In figure A.8 a) the z -scan exhibits a maximum when the mirror surface is in focus. Interestingly the maximum has a two peak structure, both are equally high and separated by 2.2 μm as can be read from the high resolution measurement in the inset. A z -misalignment of the half of this value between the foci of laser excitation and light detection can explain this feature. Figures A.8 b) and c) show the laser back ground calibration measurement for two configurations, the first without and the second with the 645 nm longpass filter. The effect of the additional filter is further suppression factor of 3. For better comparison three data sets are shown in each calibration graph for the three characteristic positions of local peaks and local minimum close to the mirror surface.

A. Laser Characteristics

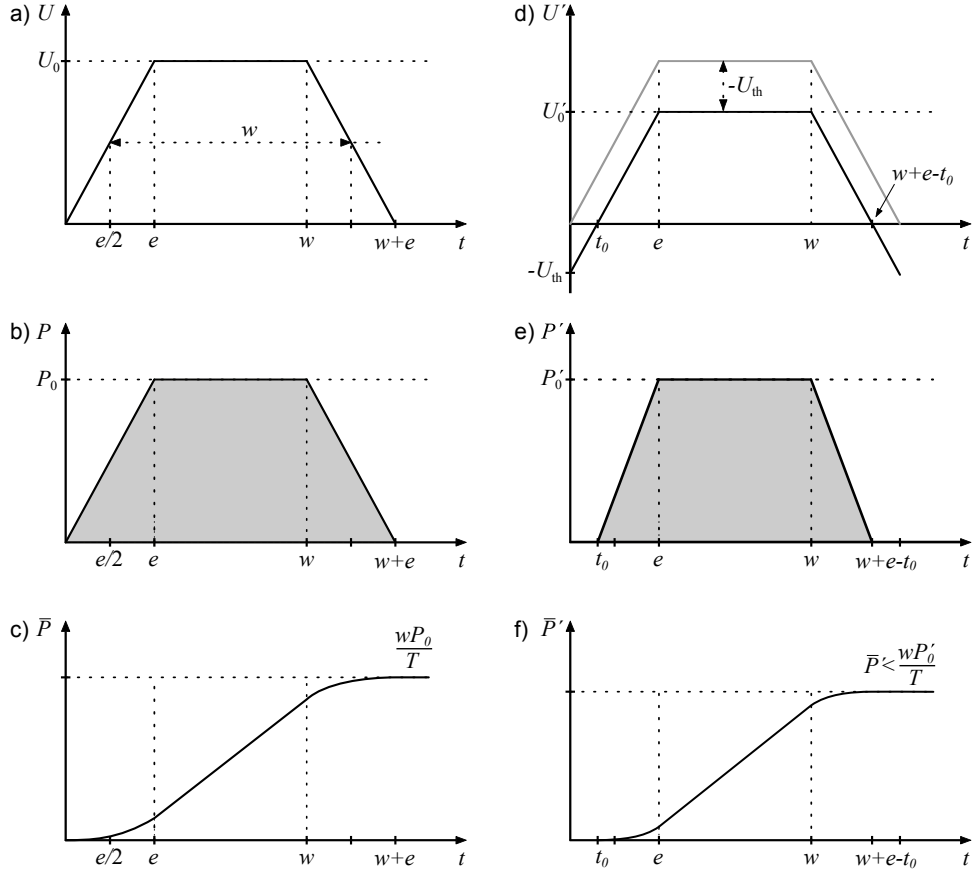


Figure A.1.: Averaged laser power for a rectangular pulse with finite pulse flanks. a) Signal as is drives the laser diode and b) simplistic assumption for laser output power and c) averaged value. d), e) Since lasing occurs only above U_{th} the effective interval of lasing is shortened. The effect can be better described by introducing U' and P' with proportional relation. f) The average laser power is lowered by a factor depending on the edge time and lasing threshold.

A.3. Laser Suppression in the Photon Detection System

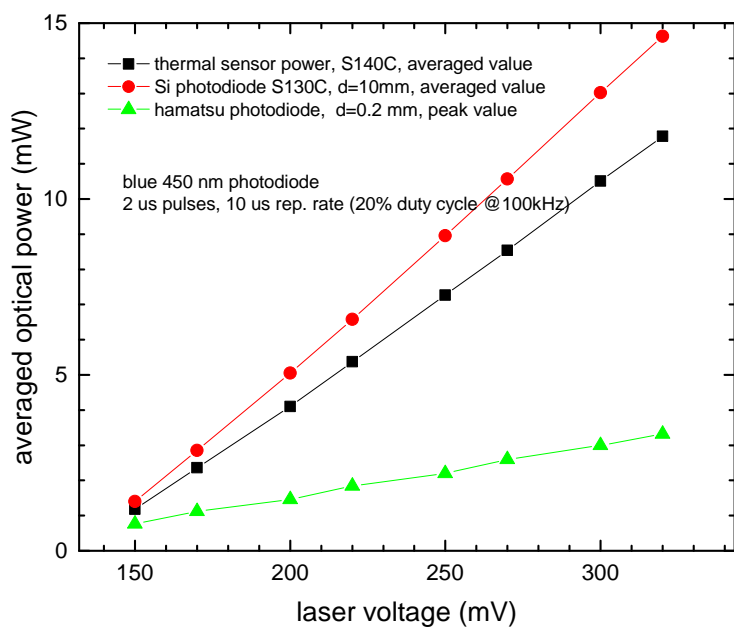


Figure A.2.: Sensors used for determination of laser powers in the setup. The fast Si diode was mainly used for pulse shape analysis rather than absolute measurements.

A. Laser Characteristics

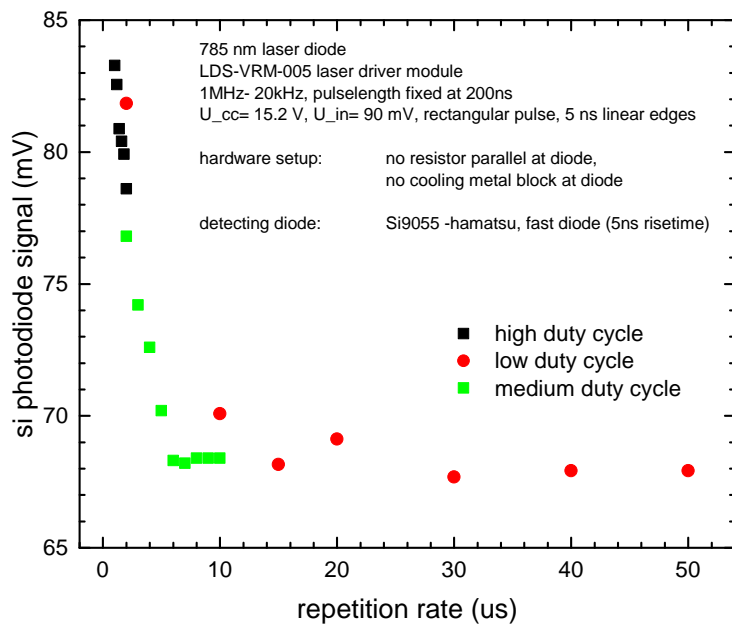


Figure A.3.: For low repetition rates at fixed pulse duration, i.e. high duty cycles a non linear increase in lasing power is observed. This effect is attributed to the laser driver.

A.3. Laser Suppression in the Photon Detection System

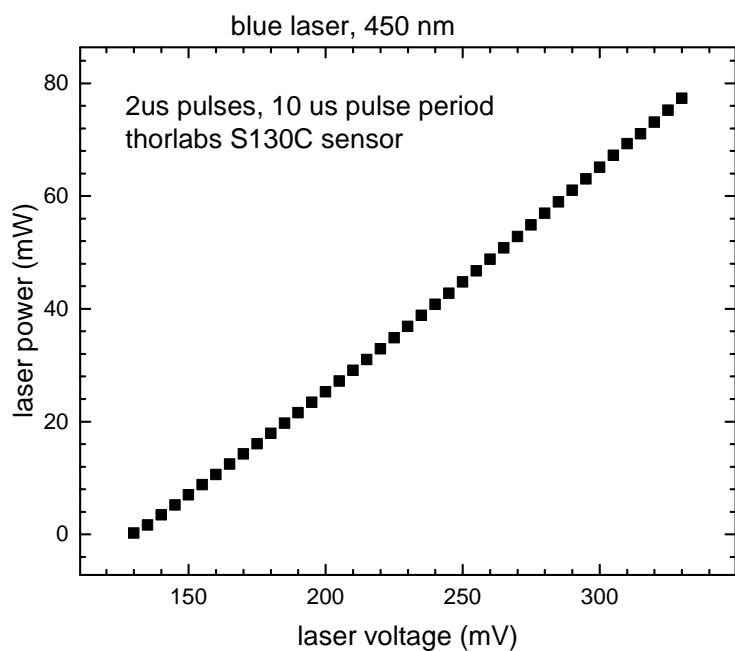


Figure A.4.: Power calibration for the 450 nm laser for long pulse operation.

A. Laser Characteristics

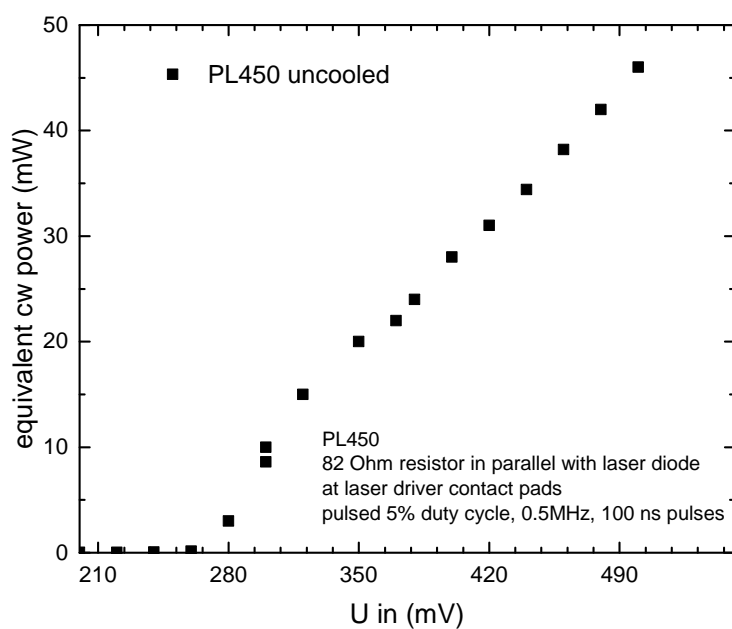


Figure A.5.: 450 nm Laser characteristics for as is was used for pulsed experiments. Intensity is measured with the S130C sensor. The laser power settled at an equilibrium value after several seconds after switch on, when the laser diode temperature saturated. Here, no cooling fan is used.

A.3. Laser Suppression in the Photon Detection System

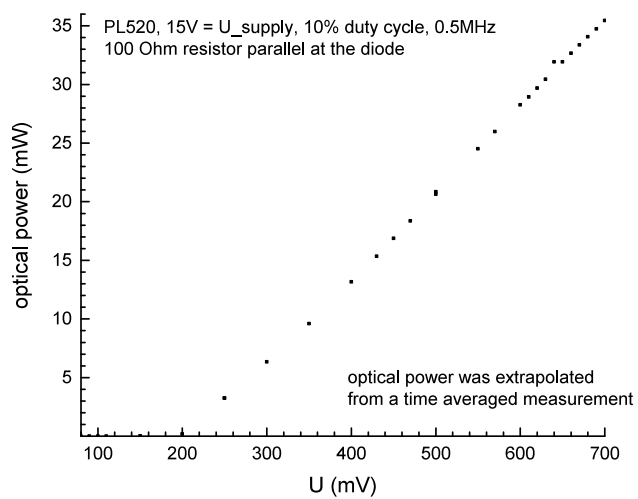
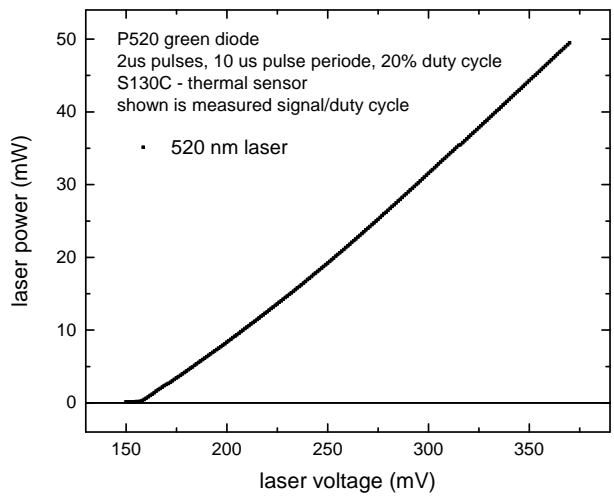


Figure A.6.: Characteristics of the 520 nm laser. a) Performance in long pulse mode operation and b) under standard experimental conditions. 75

A. Laser Characteristics

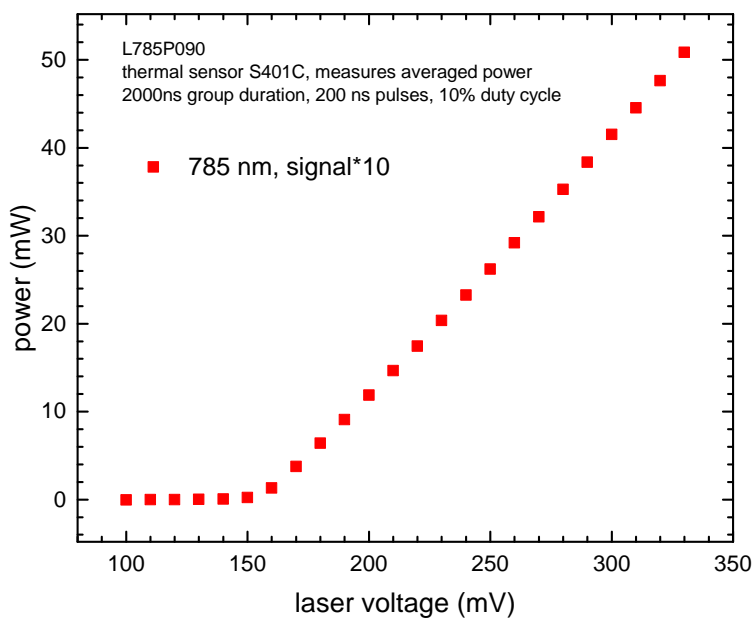


Figure A.7.: Characterization of the NIR laser. In the limit of long laser pulses and low duty cycle the 785 nm has a linear output power above the lasing threshold of 155 mV.

A.3. Laser Suppression in the Photon Detection System

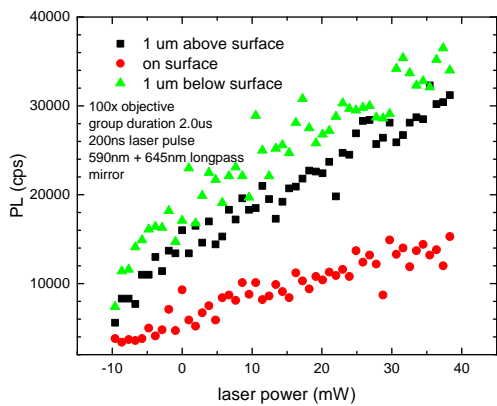
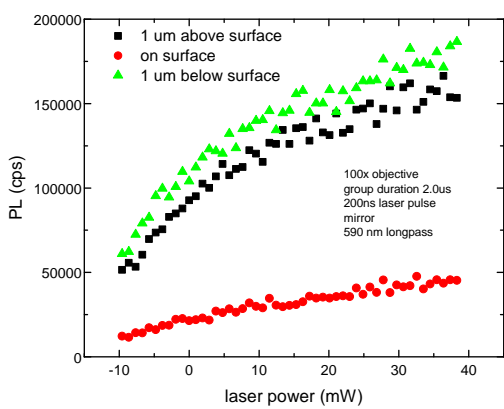
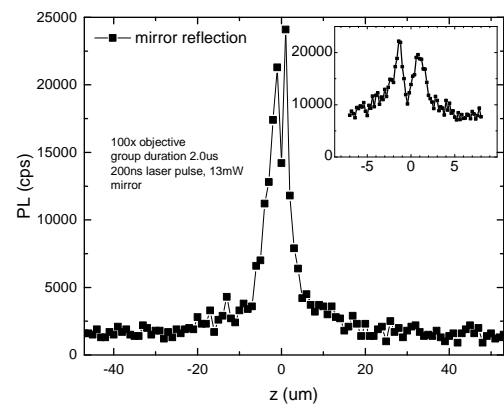


Figure A.8.: Laser reflections from a mirror in focus are not suppressed perfectly by the APD filters. Nominal laser power is plotted versus PL signal.

Bibliography

- V. M. Acosta, E. Bauch, M. P. Ledbetter, A. Waxman, L.-S. Bouchard and D. Budker: *Temperature Dependence of the Nitrogen-Vacancy Magnetic Resonance in Diamond*, Phys. Rev. Lett. **104**, 070801 (2010a).
- V. M. Acosta, A. Jarmola, E. Bauch and D. Budker: *Optical properties of the nitrogen-vacancy singlet levels in diamond*, Phys. Rev. B **82**, 201202 (2010b).
- N. Aslam, G. Waldherr, P. Neumann, F. Jelezko and J. Wrachtrup: *Photo-induced ionization dynamics of the nitrogen vacancy defect in diamond investigated by single-shot charge state detection*, New Journal of Physics **15**, 013064 (2013).
- N. Bar-Gill, L. M. Pham, A. Jarmola, D. Budker and R. L. Walsworth: *Solid-state electronic spin coherence time approaching one second*, Nature Communications **4**, 1743 EP (2013), article.
- N. Bar-Gill and A. Retzker: *Observing chemical shifts from nanosamples*, Science **357**, 38 (2017).
- K. Beha, A. Batalov, N. B. Manson, R. Bratschitsch and h. Leitenstorfer, A.: *Optimum Photoluminescence Excitation and Recharging Cycle of Single Nitrogen-Vacancy Centers in Ultrapure Diamond*, Phys. Rev. Lett. **109**, 097404 (2012).
- E. Bourgeois, A. Jarmola, P. Siyushev, M. Gulka, J. Hruby, F. Jelezko, D. Budker and M. Nesladek: *Photoelectric detection of electron spin resonance of nitrogen-vacancy centres in diamond*, Nature Communications **6**, 8577 (2015).
- E. Bourgeois, E. Londero, K. Buczak, J. Hruby, M. Gulka, Y. Balasubramanian, G. Wachter, J. Stursa, K. Dobes, F. Aumayr, M. Trupke, A. Gali and M. Nesladek: *Enhanced photoelectric detection of NV magnetic resonances in diamond under dual-beam excitation*, Phys. Rev. B **95**, 041402 (2017).

Bibliography

- A. Brenneis, L. Gaudreau, M. Seifert, H. Karl, M. S. Brandt, H. Huebl, J. A. Garrido, K. H. L. and A. W. Holleitner: *Ultrafast electronic readout of diamond nitrogen-vacancy centres coupled to graphene*, Nat Nano **10**, 135 (2015), letter.
- J. Chen, S. Lourette, K. Rezai, T. Hoelzer, M. Lake, M. Nesladek, L.-S. Bouchard, P. Hemmer and D. Budker: *Optical quenching and recovery of photoconductivity in single-crystal diamond*, Applied Physics Letters **110**, 011108 (2017).
- J. T. Choy, I. Bulu, B. J. M. Hausmann, E. Janitz, I.-C. Huang and M. Lončar: *Spontaneous emission and collection efficiency enhancement of single emitters in diamond via plasmonic cavities and gratings*, Applied Physics Letters **103**, 161101 (2013).
- D. J. Christle, A. L. Falk, P. Andrich, P. V. Klimov, J. U. Hassan, N. T. Son, E. Janzén, T. Ohshima and D. D. Awschalom: *Isolated electron spins in silicon carbide with millisecond coherence times*, Nature materials **14**, 160 (2015).
- F. Fuchs, B. Stender, M. Trupke, D. Simin, J. Pflaum, V. Dyakonov and G. V. Astakhov: *Engineering near-infrared single-photon emitters with optically active spins in ultrapure silicon carbide*, Engineering near-infrared single-photon emitters with optically active spins in ultrapure silicon carbide, Applied Physics Letters **6**, 7578 (2017).
- A. Gali: *Time-dependent density functional study on the excitation spectrum of point defects in semiconductors*, physica status solidi (b) **248**, 1337 (2011).
- A. Gruber, A. Dräbenstedt, C. Tietz, L. Fleury, J. Wrachtrup and C. Von Borczyskowski: *Scanning confocal optical microscopy and magnetic resonance on single defect centers*, Science **276**, 2012 (1997).
- W. Götz, A. Schöner, G. Pensl, W. Suttrop, W. J. Choyke, R. Stein and S. Leibenzeder: *Nitrogen donors in 4H-silicon carbide*, Journal of Applied Physics **73**, 3332 (1993).
- T. C. Hain, F. Fuchs, V. A. Soltamov, P. G. Baranov, G. V. Astakhov, T. Hertel and V. Dyakonov: *Excitation and recombination dynamics of vacancy-related spin centers in silicon carbide*, Journal of Applied Physics **115**, 133508 (2014).

Bibliography

- M. V. Hauf, P. Simon, N. Aslam, M. Pfender, P. Neumann, S. Pezzagna, J. Meijer, J. Wrachtrup, M. Stutzmann, F. Reinhard et al.: *Addressing single nitrogen-vacancy centers in diamond with transparent in-plane gate structures*, Nano letters **14**, 2359 (2014).
- D. A. Hopper, R. R. Grote, A. L. Exarhos and L. C. Bassett: *Near-infrared-assisted charge control and spin readout of the nitrogen-vacancy center in diamond*, Phys. Rev. B **94**, 241201 (2016).
- F. M. Hrubesch, G. Braunbeck, M. Stutzmann, F. Reinhard and M. S. Brandt: *Efficient Electrical Spin Readout of NV⁻ Centers in Diamond*, Phys. Rev. Lett. **118**, 037601 (2017).
- J. Isberg, J. Hammersberg, E. Johansson, T. Wikström, D. J. Twitchen, A. J. Whitehead, S. E. Coe and G. A. Scarsbrook: *High carrier mobility in single-crystal plasma-deposited diamond*, Science **297**, 1670 (2002).
- K. M. Itoh and H. Watanabe: *Isotope engineering of silicon and diamond for quantum computing and sensing applications*, MRS Communications **4**, 143–157 (2014).
- H. Kawarada: *Hydrogen-terminated diamond surfaces and interfaces*, Surface Science Reports **26**, 205 (1996).
- MaletinskyP., HongS., G. S., HausmannB., L. D., W. L., LoncarM. and YacobyA.: *A robust scanning diamond sensor for nanoscale imaging with single nitrogen-vacancy centres*, Nat Nano **7**, 320 (2012).
- J. Maze, A. Gali, E. Togan, Y. Chu, A. Trifonov, E. Kaxiras and M. Lukin: *Properties of nitrogen-vacancy centers in diamond: the group theoretic approach*, New Journal of Physics **13**, 025025 (2011).
- J. T. Muhonen, J. P. Dehollain, A. Laucht, F. E. Hudson, R. Kalra, T. Sekiguchi, K. M. Itoh, D. N. Jamieson, J. C. McCallum, A. S. Dzurak and A. Morello: *Storing quantum information for 30 seconds in a nanoelectronic device*, Nat Nano **9**, 986 (2014), letter.
- E. Rohrer: *Photoleitungs-Spektroskopie an Diamant* (Schriftenreihe des Walter Schottky Instituts, 1998).
- B. J. Shields, Q. Unterreithmeier, N. De Leon, H. Park and M. D. Lukin: *Efficient readout of a single spin state in diamond via spin-to-charge conversion*, Physical review letters **114**, 136402 (2015).

Bibliography

- P. Siyushev, H. Pinto, M. Vörös, A. Gali, F. Jelezko and J. Wrachtrup: *Optically Controlled Switching of the Charge State of a Single Nitrogen-Vacancy Center in Diamond at Cryogenic Temperatures*, Phys. Rev. Lett. **110**, 167402 (2013).
- P. L. Stanwix, L. M. Pham, J. R. Maze, D. Le Sage, T. K. Yeung, P. Cappellaro, P. R. Hemmer, A. Yacoby, M. D. Lukin and R. L. Walsworth: *Coherence of nitrogen-vacancy electronic spin ensembles in diamond*, Phys. Rev. B **82**, 201201 (2010).
- S. M. Sze and K. N. Kwok: *Semiconductor Devices* (Wiley, 2007).
- J. Walker: *Optical absorption and luminescence in diamond*, Reports on Progress in Physics **42**, 1605 (1979).
- J. Zheng, A. C. Liapis, E. H. Chen, C. T. Black and D. Englund: *Near-unity collection efficiency from quantum emitters in bulk diamond using chirped circular dielectric gratings*, arXiv preprint arXiv:1706.07566 (2017).